# Multi-omics analysis of glutamine and fish collagen peptides in alleviating post-antibiotic *Streptococcus pneumoniae* injury in feline lung cells

HUASONG BAI[1], TONG LIU[1], HENGYAN WANG[1], HONGCHEN JIN[1], YUNLIANG LI[2] and ZHANZHONG WANG[1]

[1]Nourse Science Centre for Pet Nutrition, Wuhu, Anhui 241200, P.R. China;
[2]School of Food and Biological Engineering, Jiangsu University, Zhenjiang, Jiangsu 212013, P.R. China

Received October 21, 2025; Accepted March 2, 2026

DOI: 10.3892/etm.2026.13143

**Abstract.** *Streptococcus pneumoniae* (SP) infection often leads to persistent lung injury even after antibiotic treatment. Despite this phenomenon, the mechanisms underlying host cell recovery remain poorly understood. Upon breaching the epithelial barrier, SP primarily targets the pulmonary interstitial cells, which constitute the major mesenchymal component of the lung. These cells serve as essential effectors of tissue repair, extracellular matrix remodeling and epithelial restoration. Therefore, a feline pulmonary interstitial cell (FCA-L2) model of SP infection was established to investigate the protective effects of glutamine (GLU) and fish collagen peptides (FCP) through integrated transcriptomic and metabolomic analyses. Cells were infected with SP (0.05 McFarland units for 4 h) and then treated with doxycycline (7.5 $\mu$g/ml for 18 h) followed by GLU (40 mM) or FCP (500 $\mu$g/ml). Notably, SP infection increased lactate dehydrogenase (LDH) release by 3.5-fold, induced secretion of IL-1β, TNF-α and IL-8, disrupted tight-junction proteins (claudin, ZO-1 and occludin) and caused oxidative imbalance and apoptosis despite antibiotic (doxycycline) treatment. However, treatment with GLU or FCP significantly reduced LDH release by ~40%, restored junctional proteins, suppressed inflammatory cytokines and enhanced antioxidant enzyme activities. Multi-omics analysis revealed that GLU promoted amino acid biosynthesis and energy metabolism and suppressed aminoacyl-tRNA synthetases and cell-cycle regulators, thereby enhancing metabolic adaptability. By contrast, FCP activated amino and nucleotide sugar metabolism, increased polyunsaturated fatty-acid synthesis and supported glycocalyx repair and membrane reconstruction. GLU and FCP provided complementary metabolic and structural protection, which mitigated post-infectious stress and promoted cellular recovery. The findings of the present study underscore the potential of bioactive food-derived compounds as adjunctive therapies that may accelerate lung tissue repair and enhance the efficacy of conventional antibiotics.

## Introduction

Inflammatory lung injury is a notable cause of acute respiratory disease and mortality commonly induced by bacterial pathogens [such as *Streptococcus pneumoniae* (SP) and *Staphylococcus aureus*], viral pathogens (such as SARS-CoV-2 and influenza) or mixed infections (1,2). SP remains the leading bacterial pathogen in community-acquired pneumonia (CAP). CAP is frequently associated with severe complications, such as parapneumonic effusion, empyema, necrotizing pneumonia and acute respiratory distress syndrome (ARDS) (3,4). In veterinary practice, SP is increasingly recognized as a pathogen contributing to feline lower respiratory tract infections (5). Despite the effectiveness of antibiotics in pathogen clearance, residual lung injury and secondary inflammation often persist post-infection, as exemplified by post-COVID-19 pulmonary syndromes (2,6). The sequelae as a result of bacterial pneumonia are characterized by endothelial and epithelial cell death, junctional disruption and leukocyte infiltration, which ultimately impair nutrient and gas exchange (7-10). These outcomes highlight a notable gap in the understanding of host recovery mechanisms beyond microbial eradication.

Although extensive studies have elucidated the pathogenesis of pneumonia and antimicrobial strategies, the resolution phase, particularly the mechanisms of host cellular recovery following infection, has received less attention. Alveolar epithelial regeneration, macrophage turnover and metabolic reprogramming in tissue repair are essential in ARDS, ventilator-induced lung injury and post-viral pneumonia (6,11,12). However, to the best of our knowledge, specific investigations

---

*Correspondence to:* Professor Zhanzhong Wang, Nourse Science Centre for Pet Nutrition, Floor 1, Building 3, Pet Products Industrial Base, Fanchang Economic Development Zone, 8 Yinhe Avenue, Wuhu, Anhui 241200, P.R. China
E-mail: wzz7698@tju.edu.cn

Professor Yunliang Li, School of Food and Biological Engineering, Jiangsu University, 301 Xuefu Road, Zhenjiang, Jiangsu 212013, P.R. China
E-mail: liyunliang@ujs.edu.cn

*Key words:* *Streptococcus pneumoniae*, feline, lung mesenchymal cells, glutamine, fish collagen peptides, post-infectious repair

upon SP-induced epithelial or mesenchymal injury and the ensuing host-driven reparative responses remain scarce. Notably, systematic analysis of post-SP metabolic reprogramming and membrane repair, especially in felines, is lacking.

Glutamine (GLU) is a conditionally essential amino acid that plays notable roles in redox homeostasis, nucleotide biosynthesis and immunoregulation under stress or injury. GLU preserves epithelial barrier integrity and prevents oxidative damage in pulmonary and intestinal models (13-16); however, its efficacy in bacterial pneumonia, especially its role in coordinating metabolic recovery, redox balance and cell survival after SP-induced lung damage, remains undefined.

Fish collagen peptides (FCP) are bioactive oligopeptides derived from enzymatically hydrolyzed marine byproducts possessing promising regenerative and anti-inflammatory properties. FCP acts by inhibiting MAPK pathways, activating mannose receptors and modulating Wnt/β-catenin signaling, and has demonstrated benefits in epithelial repair, skin regeneration and macrophage polarization (17-21). Nonetheless, to the best of our knowledge, their role in bacterial lung infections, including their reparative or synergistic effects in SP-induced epithelial damage, is unexplored.

Pulmonary interstitial cells of mesenchymal lineage play a notable role in lung tissue repair, extracellular matrix (ECM) remodeling and epithelial recovery following injury (22). Epithelial cells are the primary targets of bacterial infection, but mesenchymal cells are indispensable in the subsequent repair processes. Mesenchymal cells synthesize ECM components, such as collagen, cadherins, claudins and fibronectin, which are essential for tissue regeneration and structural restoration after damage (23). Moreover, they promote epithelial recovery through paracrine signaling, secreting growth factors and cytokines that stimulate epithelial cell proliferation, migration and restoration of barrier integrity (22,24,25). The interaction between mesenchymal and epithelial cells during the repair process is crucial for maintaining lung function after infection. Mesenchymal cells thus serve as an ideal *in vitro* model for investigating reparative mechanisms during the post-infectious recovery phase following bacterial lung injury because of their central role in tissue regeneration and ECM remodeling. Their ability to modulate inflammation, ECM composition and cell-cell interactions directly influences the resolution of infection-induced damage and supports lung tissue recovery.

In the present study, a feline pulmonary mesenchymal cell model (FCA-L2) of SP infection was established, followed by integrative transcriptomic and metabolomic analyses to delineate the molecular landscape of infection-induced injury to address the existing knowledge gaps. This study aimed to delineate SP-induced injury patterns and evaluate the efficacy of GLU and FCP in promoting recovery by modulating metabolism, inflammation and structural restoration.

## Materials and methods

*Materials and reagents*. L-glutamine (GLU, purity >99%) and doxycycline hydrochloride (Dox, purity >98%) were sourced from Shanghai Macklin Biochemical Co., Ltd. Fish scale-derived collagen peptides (FCP), with a molecular weight of <5,000 Da and peptide content >98%, were purchased from Hainan Huayan Collagen Technology Co., Ltd. Supplementary Tables SI and SII details the molecular weight distribution and fully hydrolyzed amino acid composition of FCP. SP (Klein) Chester (ATCC 6305) was acquired from the American Type Culture Collection. All compounds (GLU, FCP and Dox) were dissolved in phenol red-free Minimum Essential Medium (MEM, Procell, Life Science & Technology Co., Ltd.) before use.

*Cell culture and viability assay*. Feline pulmonary interstitial cells (FCA-L2), which represented fibroblast-like stromal cells of mesenchymal lineage, were obtained from the PETCC cell bank (https://www.petcc.org/). The cells were cultured in Dulbecco's modified Eagle's medium (DMEM) supplemented with 10% fetal bovine serum (FBS; Gibco; Thermo Fisher Scientific, Inc.) and maintained in a humidified incubator at 37.5˚C and 5% $CO_2$. Cell viability was confirmed using trypan blue exclusion prior to experiments.

Based on published literature (26-28) and preliminary laboratory screenings, concentration ranges for GLU (0-80 mM) and FCP (0-1,000 $\mu$g/ml) were selected to determine the optimal working doses. The cells were then seeded into 96-well plates at a density of 3x$10^5$ cells/ml for adherence for 24 h at 37.5˚C, after which various concentrations of GLU and FCP were added for an additional 24 h at 37.5˚C. Treatment media were subsequently removed, and 110 $\mu$l of phenol red-free MEM containing 10% Cell Counting Kit-8 (CCK-8; Beyotime Biotechnology) was added to each well. The plates were gently shaken for 30 sec, then incubated for 2 h at 37˚C. Absorbance of the cells was measured at 450 nm using a microplate reader. Cells cultured in MEM alone (without treatment) served as the negative control (NC).

*Lactate dehydrogenase (LDH) release assay for SP-infected lung cells*. The infection duration and bacterial concentration were optimized to establish a stable SP infection model in feline lung cells. LDH release was employed as a reliable indicator of membrane damage due to the interference of bacteria with CCK-8 detection (29). SP (ATCC 6305) was cultured in brain heart infusion broth (Qingdao Hope Bio-technology Co., Ltd.) at 37˚C and 5% $CO_2$ for 24 h. The bacteria were harvested by centrifugation at 3,000 x g for 10 min at 4˚C, and the resulting pellet was resuspended in MEM. The suspension was then adjusted to a turbidity of 0.0-0.05 McFarland (McF) units using a calibrated turbidimeter (cat. no. WGZ-1M16100; Shanghai Precision Instruments, Co., Ltd.). FCA-L2 cells were seeded in 96-well plates (3x$10^4$ cells/well) and incubated at 37.5˚C for 24 h. A total of two control groups were established: A NC group (cells incubated with MEM only) and an NC + Dox group (cells treated with 7.5 $\mu$g/ml Dox without SP infection) to evaluate potential antibiotic-induced toxicity. To optimize infection conditions, cells were exposed to SP at 0.02 or 0.05 McF for 2 or 4 h. Following infection, the medium was replaced with MEM containing 7.5 $\mu$g/ml Dox (2x) to inhibit further bacterial growth, and cells were incubated for an additional 18 h at 37.5˚C. Furthermore, to characterize the temporal progression of post-antibiotic injury, a time-course experiment was performed. Cells were infected with 0.05 McF SP for 4 h, followed by Dox treatment (7.5 $\mu$g/ml) for 12, 18, 24 or 30 h at 37.5˚C before supernatant collection. At each designated time point, plates were centrifuged at 1,000 x g for 5 min at 4˚C, and 100 $\mu$l of supernatant was collected.

LDH release was determined using a commercial kit (C0017; Beyotime Biotechnology). Briefly, LDH working solution (50 $\mu$l), containing lactate, iodonitrotetrazolium chloride and lipoamide dehydrogenase, was added to each well containing 100 $\mu$l of supernatant and incubated at room temperature for 30 min. Absorbance at 490 nm was measured using a microplate reader (SpectraMax; Molecular Devices, LLC).

*Evaluation of pharmacological intervention*. The effects of GLU and FCP on SP-induced injury in FCA-L2 cells were evaluated based on the LDH release. Briefly, 2x concentrations of GLU and FCP were prepared in MEM containing 7.5 $\mu$g/ml Dox (2x Dox-MEM). FCA-L2 cells were seeded in 96-well plates (3x$10^4$ cells/well) and incubated for 24 h at 37.5˚C, after which 100 $\mu$l of 0.05 McF SP suspension was added and the cells incubated for 4 h at 37.5˚C for infection to take place. GLU- or FCP-containing Dox-MEM (100 $\mu$l) was then added, and the cells were incubated for an additional 18 h at 37.5˚C. Cells treated with MEM alone served as the NC, whereas those treated with Dox-MEM alone served as the antibiotic control. Supernatants were subsequently collected for LDH measurement. The concentration with the greatest reduction in LDH release (GLU, 40 mM; FCP, 500 $\mu$g/ml) was used in subsequent experiments.

*Collection of whole cell lysates of differentially treated FCA-L2 cells*. A total of four treatment groups were established: NC (MEM only), SP infection (SP), GLU treatment (SP + GLU, 40 mM) and FCP treatment (SP + FCP, 500 $\mu$g/ml). FCA-L2 cells were seeded into 6-well plates (6x$10^5$ cells/well), with and without glass coverslips, and incubated at 37.5˚C for 24 h. The cells were subsequently treated with 1 ml of 0.05 McF SP suspension for 4 h, followed by 1 ml of Dox-MEM containing 80 $\mu$M GLU or 1,000 $\mu$g/ml FCP at 37.5˚C for 18 h. The SP group received Dox-MEM without functional compounds, whereas the NC group received MEM only. Cell supernatants were directly collected after treatment for subsequent assays. The supernatant was centrifuged at 9,400 x g for 10 min to pellet detached cells, which were then resuspended in their original wells. Total protein of the FCA-L2 cells was isolated using M-PER mammalian protein extraction reagent (Thermo Fisher Scientific, Inc.), followed by incubation at 4˚C for 20 min to obtain whole-cell lysates. Alternatively, FCA-L2 cells were digested with trypsin without EDTA (0.25%) and centrifuged together with the supernatant at 400 x g for 5 min to obtain whole-cell lysates. The resulting cell pellet was used for apoptosis detection.

*Measurement of cytokines in culture supernatants*. Cytokines, including interleukin-1β (IL-1β; cat. no. ml023097-2), interleukin-8 (IL-8/CXCL8; cat. no. ml023094-2) and tumor necrosis factor-α (TNF-α; cat. no. ml035852-2) in the culture supernatants, were quantified using specific ELISA kits (Shanghai Enzyme-linked Biotechnology Co., Ltd.). A sandwich ELISA protocol was employed; briefly, 50 $\mu$l of each culture supernatant was added to 96-well plates pre-coated with capture horseradish peroxidase-conjugated detection antibodies and subsequently incubated at 37˚C for 60 min. The plates were subsequently washed five times with PBST, followed by the addition of 3,3',5,5'-tetramethylbenzidine substrate. After incubation for 15 min in the dark at 37˚C, the reaction was terminated by adding 2 M $H_2SO_4$. The absorbance of the mixture was recorded at 450 nm using a microplate reader (SpectraMax; Molecular Devices, LLC).

*Measurement of tight junction proteins*. The expression levels of tight junction-associated proteins, including E-cadherin (cat. no. ml680120), occludin (cat. no. ml847159), claudin (cat. no. ml847222) and zonula occludens-1 (ZO-1; cat. no. ml847150), were determined in whole-cell lysates using ELISA kits (Shanghai Enzyme-linked Biotechnology Co., Ltd.), following the aforementioned procedure.

*Measurement of oxidative stress markers*. Oxidative stress was evaluated by quantifying malondialdehyde (MDA), superoxide dismutase (SOD) activity, glutathione peroxidase (GPX) activity, total antioxidant capacity (T-AOC) and total oxidant status (TOS) in whole-cell lysates. Protein concentration was determined using the Pierce BCA protein assay kit (Thermo Fisher Scientific, Inc.). Whole-cell lysate samples (25 $\mu$l) were mixed with 200 $\mu$l of BCA working solution, incubated at 37˚C for 30 min, and the absorbance subsequently measured at 562 nm using a microplate reader (SpectraMax; Molecular Devices, LLC). All oxidative stress assays were strictly performed in accordance with the manufacturer's reaction protocols. MDA levels were measured using a commercial thiobarbituric acid (TBA)-based kit (cat. no. S0131S; Beyotime Biotechnology) by incubating the samples at 100˚C for 15 min, with absorbance recorded at 532 nm. SOD activity was assessed using a commercial WST-8 detection reagent containing WST-8 and xanthine oxidase (cat. no. S0101S; Beyotime Biotechnology). Briefly, whole-cell lysate samples (20 $\mu$l) were incubated with the detection reagent at 37˚C for 30 min, followed by measurement of the absorbance read at 450 nm. GPX activity was measured using a commercial DTNB colorimetric-based kit (cat. no. BC1195; Beijing Solarbio Science & Technology Co., Ltd.). Briefly, 20 $\mu$l of cell lysate was mixed with the reaction working solution according to the manufacturer's instructions and incubated at 37˚C for 5 min, followed by the addition of DTNB for color development. The absorbance was recorded at 412 nm using a microplate reader. T-AOC was determined using the $Fe^{3+}$-tripyridyltriazine (TPTZ)-based FRAP method (cat. no. BC1315-100T/96S; Beijing Solarbio Science & Technology Co., Ltd.). Briefly, whole-cell lysate samples (6 $\mu$l) were mixed with 180 $\mu$l of detection reagent, incubated at 25˚C for 10 min, followed by measurement of the absorbance at 593 nm. TOS was quantified using a commercial kit (cat. no. BC6245-100T/96S; Beijing Solarbio Science & Technology Co., Ltd.). Briefly, 30 $\mu$l of sample was mixed with 160 $\mu$l of reaction reagent 1, and the baseline absorbance at 560 nm was recorded. Subsequently, 10 $\mu$l of xylenol orange reagent (reagent 2) was added and the mixture was incubated at 37˚C for 5 min. The absorbance was then measured at 560 nm, and TOS levels were calculated according to the manufacturer's instructions.

*Analysis of cell morphology and apoptosis*. Cells on coverslips from each group were fixed with 4% paraformaldehyde

(Beyotime Biotechnology) at 25˚C for 15 min, followed by staining with crystal violet solution (Qingdao Hope Bio-technology Co., Ltd.) at 25˚C for 5 min. The cells were then rinsed thrice using PBS (2 min for each rinse), and the morphological features were subsequently examined under a light microscope (Olympus CX33; Olympus Corporation). Cell apoptosis was detected by staining the cell pellets from each group with 5 µl Annexin V-FITC and 15 µl propidium iodide (PI) solution (Beyotime Biotechnology) in the dark for 15 min at room temperature. The cells were then centrifuged at 1,000 x g for 4 min, after which a 20 µl aliquot of the stained suspension was mounted on a concave glass slide (Nantong Mevid Life Science Co., Ltd.) and examined under a fluorescence microscope (BDS400; Chongqing Aote Optical Instrument, Co., Ltd.). To quantify cell density and apoptosis intensity, the obtained images were analyzed using ImageJ software (version 1.54P; National Institutes of Health). For each group, the mean gray value was determined from at least three randomly selected fields of view. The quantitative results were then expressed as a percentage relative to the NC group, which was defined as 100%.

*RNA sequencing*

*RNA isolation and library preparation.* Total RNA was extracted from cell pellets of each treatment group for transcriptome sequencing. Briefly, the cells were lysed in TRIzol reagent (Beyotime Biotechnology), followed by phase separation using chloroform (Shanghai Macklin Biochemical Co., Ltd.) and RNA precipitation using isopropanol (Shanghai Macklin Biochemical Co., Ltd.). RNA quantity and integrity were assessed using the Agilent 5400 Bioanalyzer. Samples with an RNA Integrity Number (RIN) ≥4.0 were considered qualified for subsequent analysis. Polyadenylated mRNA was subsequently enriched from total RNA using oligo(dT)-conjugated magnetic beads (cat. no. RK20257; ABclonal Biotech Co., Ltd.). cDNA libraries were constructed using the Fast RNA-seq Lib Prep Kit V2 (cat. no. RK20306; ABclonal Biotech Co., Ltd.) according to the manufacturer's instructions. First-strand cDNA synthesis was carried out using M-MuLV reverse transcriptase, followed by RNA template removal using RNase H and second-strand synthesis using DNA polymerase I. The resulting double-stranded cDNA was subjected to end repair, A-tailing and ligation with Illumina-compatible adapters, followed by purification with AMPure XP magnetic beads (cat. no. RK20257; ABclonal Biotech Co., Ltd.). The cDNA templates were amplified by PCR using the high-fidelity PCR master mix and universal primers provided in the kit (cat. no. RK20306; ABclonal Technology Co., Ltd.). The thermocycling conditions were as follows: Initial denaturation at 98˚C for 45 sec; 12-15 cycles comprised of denaturation at 98˚C for 10 sec), annealing at 60˚C for 15 sec and extension at 72˚C for 30 sec; and a final extension at 72˚C for 1 min. The generated libraries finally underwent paired-end sequencing on an Illumina NovaSeq 6000 platform (Novogene Co., Ltd.).

*Differential expression analysis.* Raw reads were processed using fastp (v2.3; https://github.com/OpenGene/fastp/blob/master/README.md) to remove adapter sequences, undetermined bases and low-quality reads, yielding high-quality clean data. The clean reads were subsequently aligned to the Felis catus reference genome (Felis_catus_9.0; https://ftp.ncbi.nlm.nih.gov/genomes/all/GCF/000/181/335/GCF_000181335.3_Felis_catus_9.0/) using HISAT2 (v2.2; https://daehwankimlab.github.io/hisat2/). Gene-level read counts were obtained using featureCounts (v2.0; https://subread.sourceforge.net/). Gene expression levels were normalized and quantified using fragments per kilobase of transcript per million mapped (FPKM) reads. Principal component analysis (PCA) was performed based on FPKM values. Differentially expressed genes (DEGs) between groups were identified using the DESeq2 R package (v1.42.0; https://bioconductor.org/packages/release/bioc/html/DESeq2.html). Raw P-values were calculated and adjusted for multiple testing using the Benjamini-Hochberg method. Genes with an adjusted P-value (padj)≤0.05 and absolute fold change (FC)≥1.2 were considered significantly differentially expressed.

*Gene set enrichment analysis (GSEA).* GSEA was performed to identify biological pathways affected by various treatments. Notably, gene sets were annotated based on the Kyoto Encyclopedia of Genes and Genomes database (KEGG; https://www.kegg.jp/). All genes were ranked based on expression differences between groups using the Signal2Noise metric. The analysis was conducted using the GSEA desktop application (Broad Institute; http://www.broadinstitute.org/gsea). Enrichment scores were calculated via permutation testing and normalized to account for gene set size. Pathways with a false discovery rate <0.25 were considered significantly enriched.

*Untargeted metabolomics analysis.* Untargeted metabolomics profiling was performed on whole-cell lysates from each treatment group using liquid chromatography-tandem mass spectrometry (LC-MS/MS). Cells were extracted with 80% methanol, flash-frozen in liquid nitrogen and ground into powder. The ground samples were reconstituted in 10% methanol after lyophilization. Equal aliquots from all samples were pooled to generate a quality control (QC) sample, while 53% methanol was used as a blank control. Chromatographic separation was conducted on a ultra-high-performance-LC system equipped with a Hypersil GOLD C18 column (Thermo Fisher Scientific, Inc.), followed by MS detection using a Q Exactive™ HF instrument (Thermo Fisher Scientific, Inc.) operating in both positive and negative ionization modes. Chromatographic separation was performed on a Hypersil GOLD C18 column maintained at 40˚C with a constant flow rate of 0.2 ml/min. The mobile phases consisted of 0.1% formic acid in water (A) and methanol (B). A linear gradient elution was applied as follows: 98% A at 0-1.5 min, decreased to 15% A at 3 min, followed by 0% A at 10 min. The system returned to initial conditions (98% A) at 10.1 min and was re-equilibrated until 12 min. Mass spectrometric detection was performed in both positive and negative electrospray ionization modes with full MS scan ranges set from 100 to 1,500 m/z. The spray voltage was set to 3.5 kV, with a sheath gas flow rate of 35 psi and an auxiliary gas flow rate of 10 l/min. The capillary temperature was maintained at 320˚C, and the auxiliary gas heater was set to 350˚C. The S-lens RF level was configured at 60. Data acquisition was carried out in data-dependent MS/MS mode.

Raw data were processed using the XCMS software (V4.0; The Scripps Research Institute) for peak detection and quantification. Metabolite identification was performed using Novogene In-house Database (Novogene Co., Ltd.), which integrates high-resolution MS data from established chemical standards and internal reference materials. Data preprocessing, which involved filtering of the background ions using blank samples and exclusion of metabolites with a coefficient of variation >30% in QC samples, was performed in Python (v3.5; Python Software Foundation). Normalization was performed by calculating the ratio of metabolite intensities in each sample to those in QC samples. PCA was conducted using metaX (v1.4.16; BGI Genomics), followed by a calculation of the variable importance in projection (VIP) scores, FC and t-test P-values. Metabolites with VIP≥1, P<0.05 and FC≥1.5 or ≤0.67 were defined as significantly different. Volcano plots were generated using the ggplot2 package in R (v3.4.3; https://ggplot2.tidyverse.org/). Pathway enrichment analysis of differential metabolites was performed using GSEA software (gsea-3.0; Broad Institute; https://www.gsea-msigdb.org/gsea/index.jsp).

*Integrated transcriptomic and metabolomic analysis*. Integrated analysis of transcriptomic and metabolomic datasets was performed using the MetTranAnalysis module on the NovoMagic cloud platform (Novogene Co., Ltd.) to investigate post-transcriptional regulatory patterns. KEGG-based co-enrichment analysis was conducted to identify pathways jointly affected by DEGs and differential metabolites. Bubble plots of shared pathways were generated, followed by a determination of their statistical significance using Fisher's exact test (P<0.05). Gene-metabolite correlation analysis was subsequently performed to strengthen the integration at the molecular level. Genes and metabolites belonging to the enriched core KEGG pathways in each comparison group (GLU_SP vs. SP and FCP_SP vs. SP) were selected for correlation analysis. Pearson correlation coefficients were calculated using the NovoMagic platform based on log2-transformed normalized expression values of transcripts and metabolites. Correlation matrices were visualized as heatmaps to display the association patterns between key genes and metabolites.

*Statistical analysis*. Data are presented as means ± standard deviation (n≥4 biological replicates per group). Statistical analyses were performed using SPSS software (IBM Corp., version 26). Statistical differences among multiple groups were first evaluated using Levene's test to assess the homogeneity of variances. For datasets with equal variances, a one-way analysis of variance (ANOVA) followed by Tukey's post-hoc test was performed. For datasets with unequal variances, Welch's ANOVA followed by the Games-Howell post-hoc test was employed. P<0.05 was considered to indicate a statistically significant difference.

## Results

*Optimization of SP infection conditions*. The optimal SP infection condition in FCA-L2 cells was determined based on LDH release. As shown in Fig. 1A, LDH levels in the NC and NC + Dox groups were similar (100±10.10% vs. 99.54±3.90%), indicating that Dox had no effect on LDH release. SP infection at a low dose (0.02 McF) for 2 and 4 h, followed by 18 h of Dox treatment, caused only a slight increase in LDH (108.40-111.72%). By contrast, high-dose SP infection (0.05 McF) for 4 h led to a sharp increase (352.90±12.39%) despite Dox treatment, indicating persistent cytotoxicity and damage. To further clarify the temporal characteristics of post-antibiotic injury, LDH release was assessed at different time points (12, 18, 24 and 30 h) after Dox treatment following SP infection (0.05 McF, 4 h) (Fig. 1B). LDH levels remained consistently elevated at 12 h (381.46±9.27%), 18 h (352.90±7.95%) and 24 h (365.68±6.42%), but declined at 30 h (309.61±6.97%), suggesting that the 12-24 h window represents a sustained injury phase. SP infection at 0.05 McF for 4 h, followed by 18 h of Dox treatment, was selected as the standard condition for subsequent experiments to ensure feasibility.

*GLU and FCP reduced SP-induced LDH release*. As shown in Fig. 1C, CCK-8 assays demonstrated that GLU (1.25-20 mM) and FCP (31.25-500 µg/ml) had no adverse effects on FCA-L2 cell viability. Notably, higher concentrations (40-80 mM GLU and 1,000 µg/ml FCP) demonstrated slight promotive effects on cell growth, confirming their safety. Consequently, GLU (40 and 80 mM) and FCP (500 and 1,000 µg/ml) were selected for subsequent efficacy evaluations. SP infection significantly increased LDH release to 354.80±11.12% relative to NC (100%) (Fig. 1D); however, treatment with GLU reduced LDH release to 225.86±17.42% (40 mM) and 228.05±15.29% (80 mM), whereas FCP treatment reduced it to 283.85±17.93% (500 µg/ml) and 293.67±18.07% (1,000 µg/ml). These results indicate that both GLU and FCP alleviated SP-induced cytotoxicity.

*GLU and FCP reduced the levels of SP-induced inflammatory cytokines*. SP infection significantly elevated the secretion of IL-1β, TNF-α and IL-8 in the supernatant of FCA-L2 cells compared with the NC group (Fig. 1E). Treatment with GLU (40 mM) and FCP (500 µg/ml) significantly reduced the levels of all three cytokines compared with SP: IL-1β decreased from 96.96±4.66 pg/ml (SP) to 75.61±7.01 pg/ml (GLU + SP) and 72.78±3.04 pg/ml (FCP + SP); TNF-α decreased from 19.88±1.85 pg/ml to 16.72±1.07 and 17.77±1.19 pg/ml; and IL-8 decreased from 60.02±4.47 pg/ml to 55.67±2.80 and 55.07±3.77 pg/ml, respectively. These results suggest that both GLU and FCP alleviate SP-induced inflammatory responses in feline lung cells, with the most prominent effect observed on IL-1β.

*GLU and FCP restored junction protein expression suppressed by SP*. SP infection significantly reduced the expression of claudin, ZO-1, occludin and E-cadherin in FCA-L2 cells compared with NC (Fig. 1F). However, treatment with GLU (40 mM) or FCP (500 µg/ml) partially reversed these reductions. Claudin increased from 59.76 pg/mg (SP) to 74.22 (GLU + SP) and 75.56 pg/mg (FCP + SP), ZO-1 increased from 395.17 to 484.65 and 494.46 ng/mg and occludin increased from 84.39 to 99.20 and 97.49 ng/mg, respectively. Regarding E-cadherin, its expression was significantly restored by GLU treatment, increasing from 424.23 ng/mg in the SP group to 465.27 ng/mg. By contrast, although FCP treatment slightly increased E-cadherin levels to 432.62 ng/mg, this change did not reach statistical significance.

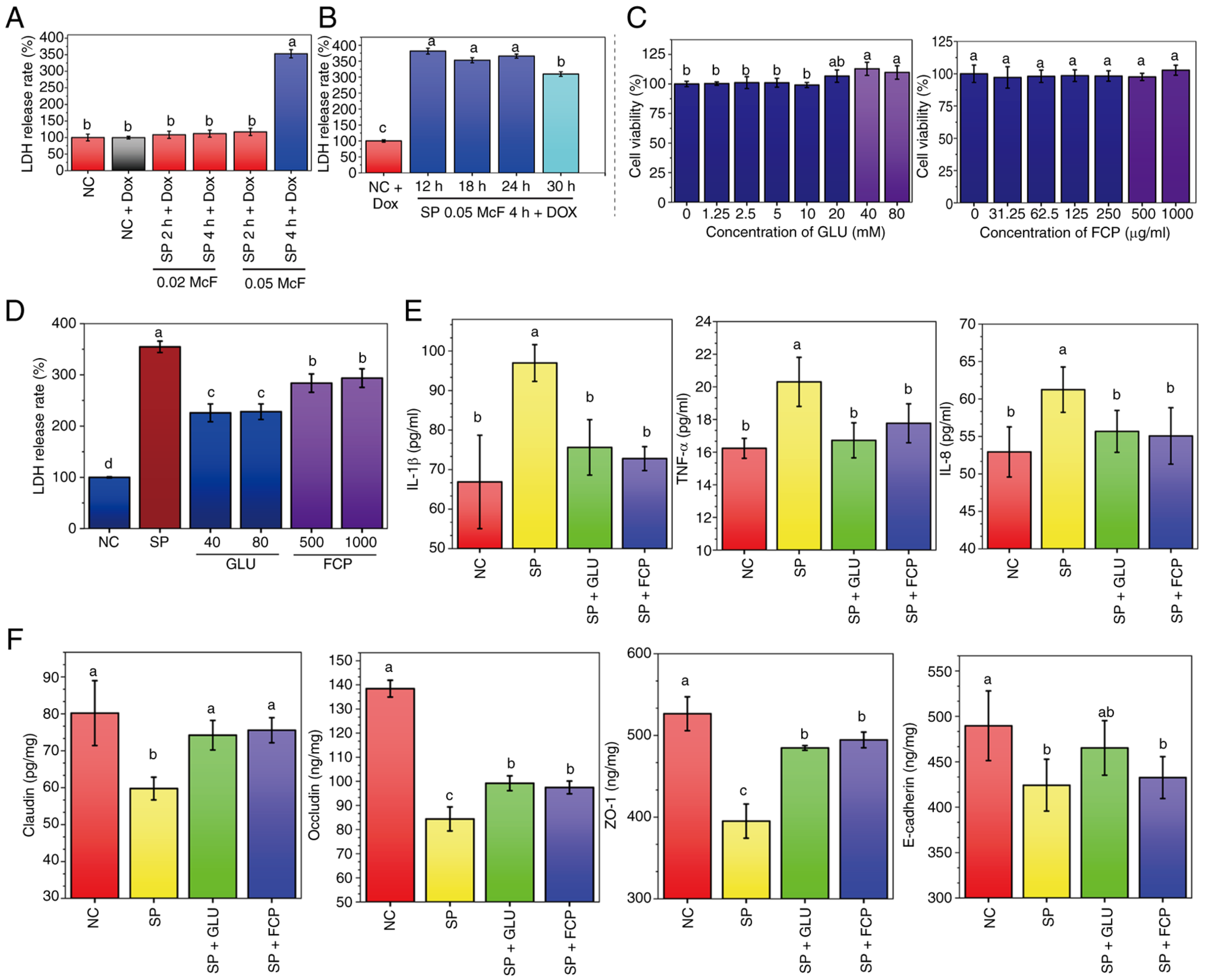

Figure 1. Effects of GLU and FCP on cytotoxicity, cytokine levels and tight junction protein expression in SP-infected feline lung FCA-L2 cells. (A) LDH release following SP infection at different durations and bacterial concentrations. NC: untreated cells in minimum essential medium; NC-Dox: cells treated with 3.75 $\mu$g/ml Dox for 18 h; SP + 2 h + Dox and SP + 4 h + Dox: SP infection for 2 or 4 h, followed by 3.75 $\mu$g/ml Dox treatment for 18 h. (B) Time-course assessment of LDH release after SP infection (0.05 McF, 4 h) followed by doxycycline treatment (3.75 $\mu$g/ml) for 12, 18, 24 or 30 h. The NC + DOX group represents uninfected cells treated with DOX for the corresponding duration. (C) Cell viability of FCA-L2 cells after treatment with different concentrations of GLU (left) or FCP (right), assessed using the Cell Counting Kit-8 assay. (D) LDH release after SP infection (4 h) followed by 18 h treatment with GLU or FCP in the presence of 3.75 $\mu$g/ml Dox. The SP group received Dox alone. (E) Levels of IL-1β, TNF-α and IL-8 in the supernatant of SP-infected cells treated with GLU (40 mM) or FCP (500 $\mu$g/ml). (F) Expression of tight junction proteins, including E-cadherin, occludin, claudin and ZO-1, after GLU or FCP treatment. All data are presented as mean ± standard deviation (n≥4 per group). Different lowercase letters (a-d) indicate significant differences ($P<0.05$), while groups sharing at least one common letter show no statistically significant difference. GLU, glutamine; FCP, fish collagen peptides; SP, *Streptococcus pneumoniae;* ZO-1, zonula occludens-1; NC, negative control; Dox, doxycycline; McF, McFarland; LDH, lactate dehydrogenase.

*GLU and FCP attenuated apoptosis and oxidative stress in SP-infected cells*. Cell morphology and apoptosis were assessed via crystal violet and Annexin V-FITC/PI staining, respectively. Notably, FCA-L2 cells in the NC group exhibited dense and orderly arrangement with tight intercellular connections. (Fig. 2A; upper and middle panels). By contrast, cells infected with SP exhibited increased staining intensity, reduced cell density and signs of shrinkage and rupture. Treatment with 40 mM GLU or 500 $\mu$g/ml FCP restored cellular morphology, reduced staining intensity and enhanced cell-to-cell contact compared with SP infected cells. Quantitative analysis of the staining showed that the relative cell density decreased from 100% (NC) to 75.57% after SP infection; however, treatment with 40 mM GLU or 500 ug/ml FCP restored cell morphology and increased the relative density to 85.89 and 88.46%, respectively.

Annexin V-FITC/PI staining (Fig. 2A, lower panel) revealed a increase in early and late apoptotic cells following SP infection, which was reduced by GLU and FCP treatment. The relative fluorescence intensity of apoptotic cells spiked from 100% (NC) to 712.12% (SP group). Notably, GLU and FCP treatment effectively mitigated this effect, reducing the intensity to 314.27 and 344.07%, respectively. Regards oxidative stress markers (Fig. 2B-E), SP infection significantly elevated MDA levels and reduced SOD and GPX activities compared with the NC group. These alterations were significantly reversed by both GLU and FCP treatment. Although the T-AOC/TOS ratio followed a downward trend after SP infection and a slight upward trend following GLU or FCP treatment, these changes did not reach statistical significance.

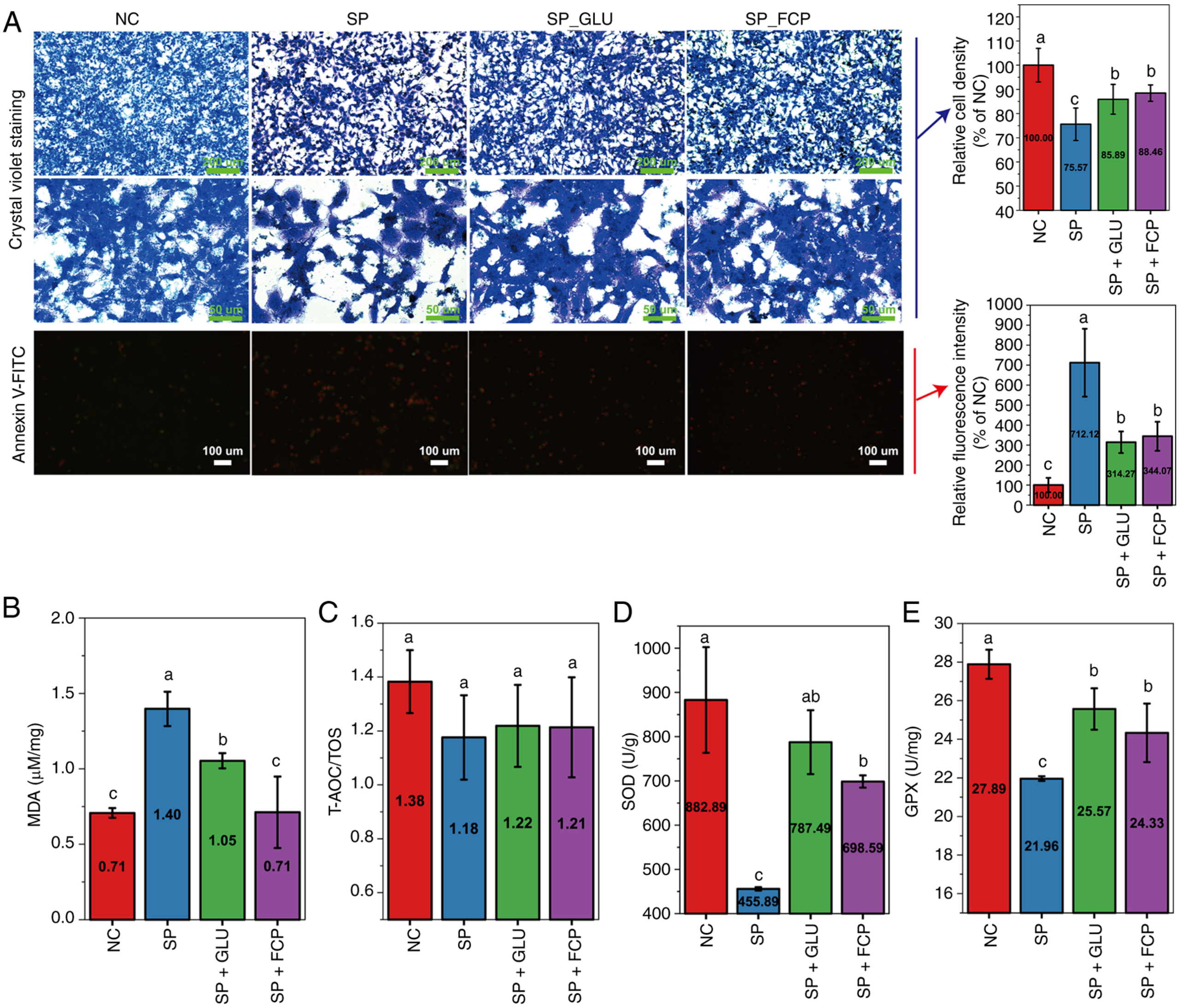

Figure 2. Effects of GLU and FCP on morphology, apoptosis and oxidative stress in SP-infected FCA-L2 cells. (A) Morphological changes (crystal violet staining, scale bars, 200 and 50 $\mu$m) and apoptosis (Annexin V-FITC/PI staining, scale bar, 100 $\mu$m) in each group following intervention with GLU (40 mM) or FCP (500 $\mu$g/ml). The right panels show the corresponding quantitative bar charts for relative cell density and the relative percentage of apoptotic cells following intervention with GLU (40 mM) or FCP (500 ug/ml). (B) MDA levels; (C) Ratio of T-AOC/TOS; (D) SOD levels; and (E) GPX levels. All data are expressed as mean ± standard deviation (n≥4 per group). Different lowercase letters (a-c) indicate significant differences ($P<0.05$), while groups sharing at least one common letter show no statistically significant difference. GLU, glutamine; FCP, fish collagen peptides; SP, *Streptococcus pneumoniae;* MDA, malondialdehyde; SOD, superoxide dismutase; MDA, malondialdehyde; T-AOC, total anti-oxidant capacity; TOS, total oxidant capacity; GPX, glutathione peroxidase.

*Transcriptomic analysis and DEG screening.* RNA sequencing was performed to assess global transcriptomic changes among NC, SP, GLU_SP and FCP_SP groups. PCA revealed distinct clustering across all four groups; there was a clear separation between SP and NC, whereas GLU_SP and FCP_SP showed partial shifts in different directions (Fig. 3A). The DEG clustering heatmap demonstrated substantial transcriptional alterations after SP infection and notable expression changes following GLU or FCP treatment (Fig. 3B). Venn analysis revealed 13,052 commonly expressed genes across groups, along with subsets of uniquely regulated genes in each treatment (Fig. 3C). SP vs. NC had 3,980 DEGs (2,045 upregulated, 1,935 downregulated), GLU_SP vs. SP had 3,321 DEGs (1,679 upregulated, 1,642 downregulated) and FCP_SP vs. SP had 2,312 DEGs (1,257 upregulated, 1,055 downregulated) (Fig. 3D). This finding suggested that both GLU and FCP modulated SP-induced transcriptomic responses.

*SP activated endocytosis and suppressed aminoacyl-tRNA biosynthesis in lung cells.* GSEA was performed to explore the transcriptional mechanisms of SP infection in FCA-L2 cells. SP significantly upregulated 'endocytosis', 'glycerophospholipid metabolism', 'sphingolipid metabolism' and 'adherens junction' pathways compared with NC. Alternatively, SP significantly downregulated the 'aminoacyl-tRNA biosynthesis' pathway compared with NC (Fig. 4A).

SP infection also significantly downregulated 14 out of 17 core genes in the aminoacyl-tRNA biosynthesis pathway (Fig. 4B). These genes included *LARS1, YARS1, MARS1, GARS1, WARS1, IARS1, CARS1, AARS1, FARSB, DARS1, EPRS1* and *TARS1*. Notably, these genes encode cytoplasmic aminoacyl-tRNA synthetases responsible for conjugating leucine, tyrosine, methionine, glycine, tryptophan, isoleucine, cysteine, alanine, phenylalanine, aspartate, glutamate, proline and threonine to their respective tRNAs (30). Mitochondrial

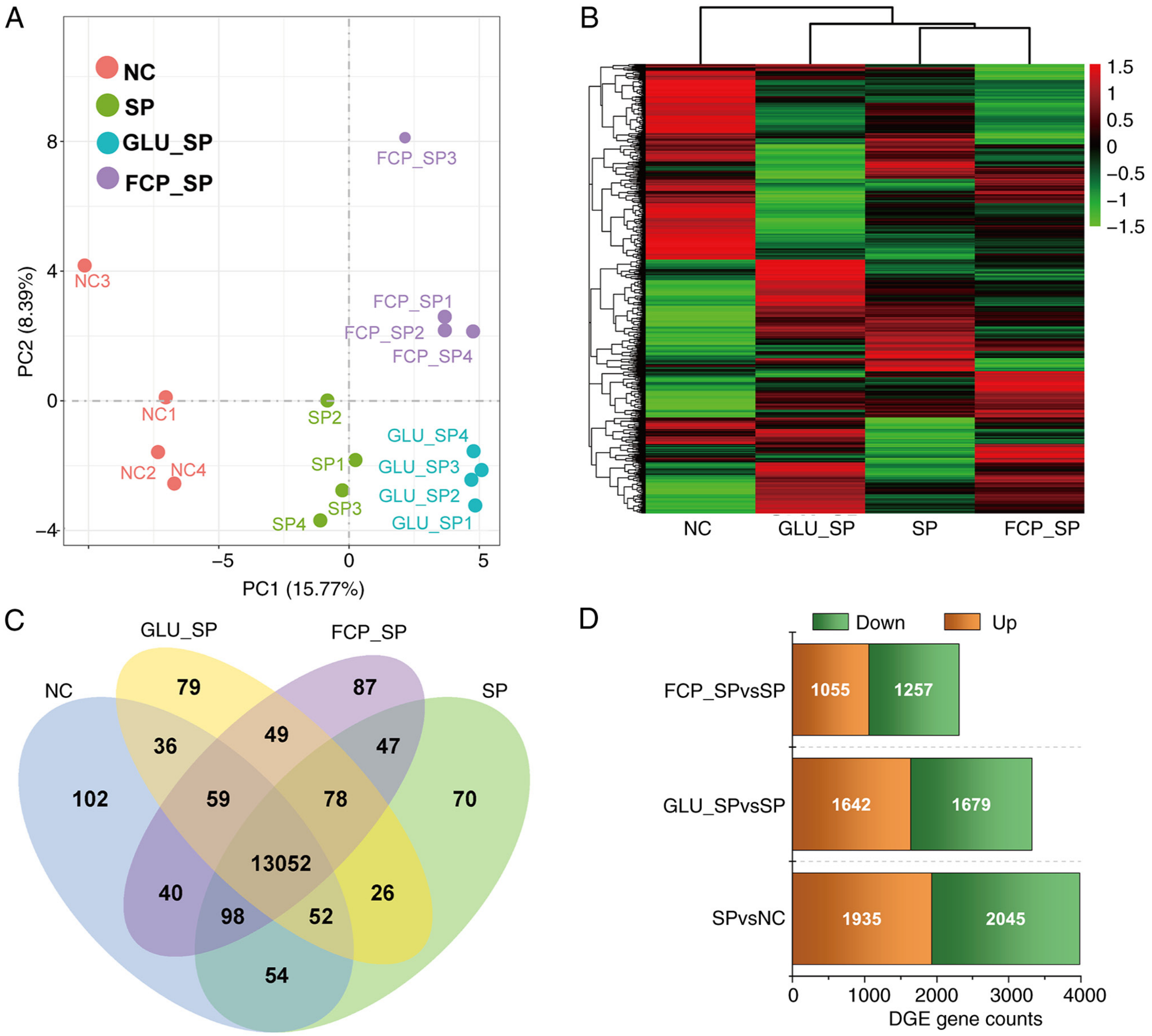

Figure 3. Transcriptomic profiling and identification of DEGs. (A) PCA showing distinct clustering among NC, SP, GLU_SP and FCP_SP groups. (B) Heatmap of DEGs based on FPKM-normalized values; columns represent sample groups and rows represent individual genes. (C) Venn diagram showing the number of unique and overlapping DEGs among groups. (D) Bar plot summarizing the number of upregulated and downregulated DEGs in each comparison. Data were based on reference-guided RNA sequencing (n=4 per group). DGES, differentially expressed genes; PCA, Principal component analysis; GLU, glutamine; FCP, fish collagen peptides; SP, *Streptococcus pneumoniae;* SOD, superoxide dismutase; MDA, malondialdehyde; NC, negative control.

synthetases *MARS2, WARS2* and *RARS2* were also suppressed, suggesting that SP impairs both cytosolic and mitochondrial protein translation. This widespread inhibition of aminoacylation potentially disrupted translational fidelity and efficiency, contributing to cellular injury and stress responses upon infection (31).

By contrast, SP infection significantly upregulated a cluster of core genes in the endocytosis pathway. The notable genes that were upregulated included *RAB11B, RAB11FIP3, RAB11FIP4* and *RAB11FIP5*, which encode notable regulators of recycling endosomes (32) (Fig. 4C). Notably, *RAB11B*, a master GTPase that controls the slow recycling of membrane proteins and receptors (33), was notably induced, suggesting it may act as a central target mediating SP-induced endocytic activation. Its interacting partners, *RAB11FIP3-5*, which facilitate cargo sorting and endosomal trafficking (34), were also elevated, indicating enhanced membrane recycling dynamics. Upregulation of *AP2A1* (clathrin adaptor complex), *DNM1* (dynamin GTPase for vesicle scission), *SH3KBP1* (endocytic scaffold protein) and *EPN1* (epsin, membrane curvature modulator) indicated activation of clathrin-mediated endocytosis. Moreover, upregulation of *ARF3*, *ARF5*, *ARFGAP1*, *EHD1* and *EHD4* provided additional evidence for the widespread activation of vesicle budding, trafficking and recycling machinery. These transcriptional changes collectively suggest that SP infection enhances endocytic trafficking and membrane turnover in lung mesenchymal cells, potentially disrupting intracellular homeostasis and facilitating pathogen-host interactions.

SP infection also significantly upregulated a cluster of genes involved in glycerophospholipid metabolism, including *GPAT3* (glycerol-3-phosphate acyltransferase), *AGPAT1* and

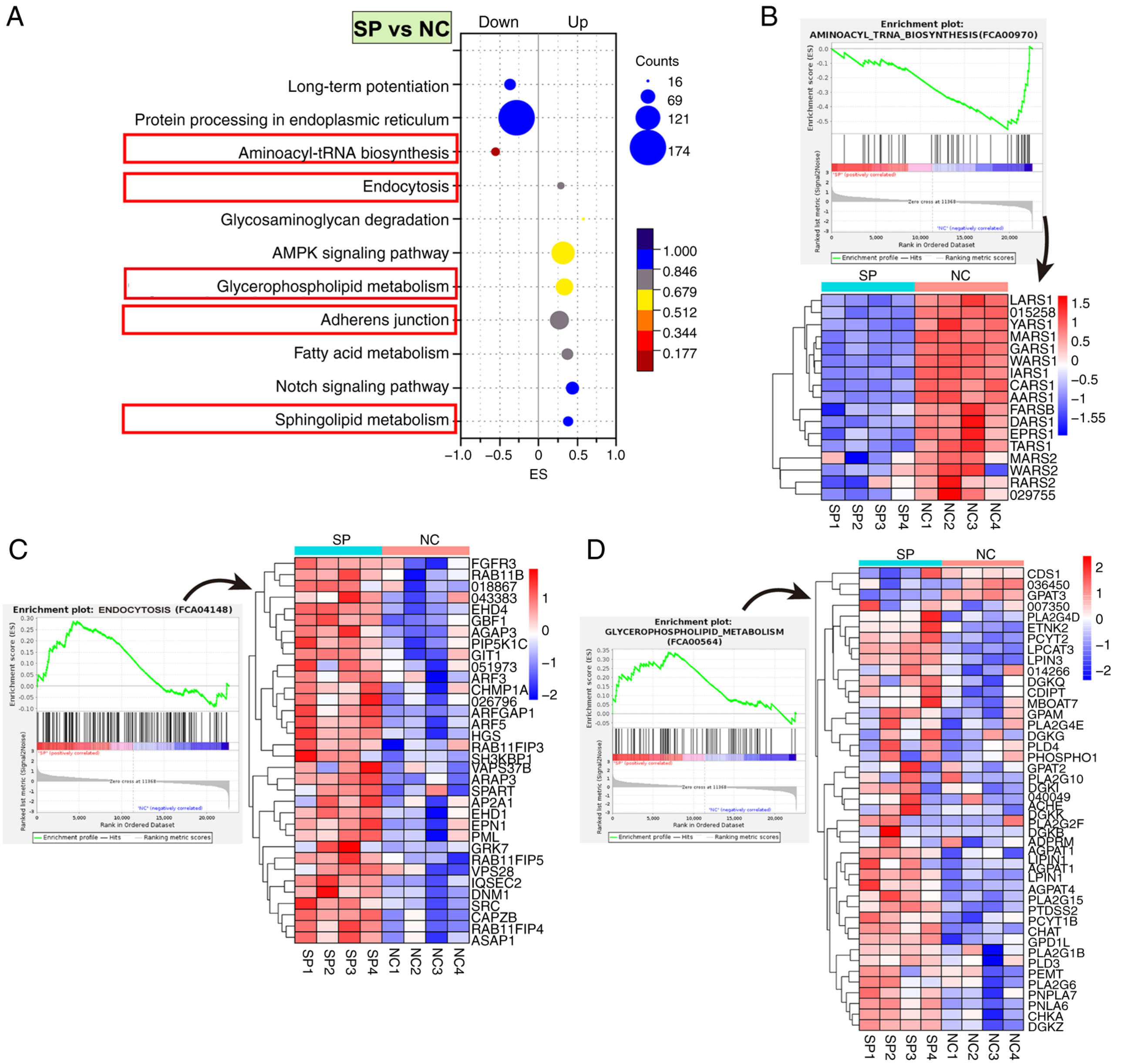

Figure 4. KEGG-GSEA enrichment analysis of SP-infected FCA-L2 cells. (A) Bubble plot of enriched KEGG pathways in SP vs. NC. The y-axis represents enriched pathways, the x-axis shows the ES, where positive values indicate upregulation and negative values indicate downregulation. Bubble size reflects the number of enriched genes and color represents the false discovery rate (q-value). (B-D) GSEA enrichment plots and heatmaps of core genes in significantly enriched pathways, including (B) aminoacyl-tRNA biosynthesis, (C) endocytosis and (D) glycerophospholipid metabolism. Upper panels show the ES curve with the peak corresponding to the pathway's ES value. Lower panels display hierarchical clustering heatmaps of leading-edge core genes in each pathway. KEGG, Kyoto Encyclopedia of Genes and Genomes; GSEA, gene set enrichment analysis; SP, *Streptococcus pneumoniae;* NC, negative control; ES, enrichment score.

*AGPAT4* (1-acylglycerol-3-phosphate O-acyltransferases) and *LPIN1* (phosphatidate phosphatase). Upregulation of these genes denoted accelerated *de novo* phosphatidic acid synthesis and triacylglycerol precursor production (35). The upregulation of *PCYT1B* and *PTDSS2*, which encode CDP-choline synthase and phosphatidylserine synthase, respectively, as well as *CHKA* (choline kinase) and *PEMT* (phosphatidylethanolamine N-methyltransferase), reflected enhanced phosphatidylcholine and phosphatidylserine biosynthesis (36). Upregulation of *DGKZ, DGKB* and *GPD1L* suggested increased diacylglycerol-phosphatidic acid interconversion and redox-linked glycerolipid flux (37,38). Enzymes involved in phospholipid hydrolysis, including *PLA2G15, PLA2G6, PLA2G1B* and *PLD3*, were also elevated, supporting intensified membrane lipid turnover. Moreover, *ADPRM* (ADP-ribose pyrophosphatase) and *CHAT* (choline acetyltransferase) were upregulated, implying altered nucleotide and acetylcholine-linked phospholipid metabolism. These transcriptional changes collectively indicated that SP infection activates glycerophospholipid remodeling through coordinated upregulation of lipid biosynthetic, hydrolytic and signaling enzymes, potentially disrupting membrane integrity and promoting inflammatory stress responses in lung mesenchymal cells.

*GLU suppressed cell cycle-related pathways in SP-infected cells*. GLU intervention (GLU_SP vs. SP) led to significant pathway remodeling (Fig. 5A), leading to downregulation of pathways, including the 'cell cycle', 'aminoacyl-tRNA biosynthesis', 'p53 signaling' and 'apoptosis', suggesting inhibition of proliferation and stress responses. By contrast, the 'biosynthesis of nucleotide sugars' and 'biosynthesis of amino sugars', as well as 'amino acid and nucleotide sugar metabolism' were significantly upregulated (Fig. 5E-F), indicating a metabolic shift toward glycan precursor generation. These changes suggested that GLU suppressed SP-induced proliferative stress while reprogramming intracellular carbohydrate metabolism.

GLU treatment led to broad suppression of core regulatory genes in the cell cycle pathway (Fig. 5B). Cyclin-dependent kinases and regulators, including *CDK1, CDK2, CDK4, CCNE2* and *CDC25B,* were downregulated, indicating inhibition of G1/S and G2/M transitions (39). Multiple DNA replication licensing and elongation factors, such as *MCM2-7, CDT1, CDC45* and *PCNA,* were also suppressed, reflecting S-phase arrest (40). In parallel, mitotic checkpoint and chromosome segregation components, including *SMC1B, SMC3, RAD21* and *TTK,* were downregulated, suggesting impaired spindle assembly and progression into mitosis (41,42). These changes collectively indicated that GLU inhibited SP-induced aberrant cell cycle progression by targeting DNA replication, checkpoint signaling and mitotic machinery in lung mesenchymal cells.

Moreover, GLU treatment suppressed a panel of cytoplasmic aminoacyl-tRNA synthetases involved in the aminoacyl-tRNA biosynthesis pathway (Fig. 5C). They included *LARS1, MARS1, GARS1, AARS1, CARS1, TARS1, FARSB* and *IARS1*, which are responsible for charging tRNAs with leucine, tyrosine, methionine, glycine, alanine, cysteine, threonine, phenylalanine and isoleucine, respectively. This coordinated repression indicated a global inhibition of tRNA aminoacylation, suggesting translational suppression and reduced protein synthesis demand under GLU treatment in SP-infected lung mesenchymal cells.

GLU treatment also led to coordinated downregulation of multiple core genes involved in DNA damage response, cell cycle arrest and apoptosis regulation in the p53 signaling pathway (Fig. 5D). Notable cyclin-dependent kinases (*CDK1, CDK2* and *CDK4*) and their regulatory cyclins (*CCNB1, CCNB2, CCNE2, CCNG1* and *CCNG2*) were suppressed, indicating a blockade of G1/S and G2/M transitions. Checkpoint kinase *CHEK1* and tumor suppressor *GADD45A*, which mediate DNA damage-induced arrest, were also downregulated. In addition, GLU reduced the expression of *RRM2* and *RRM2B* (ribonucleotide reductase subunits), *PMAIP1* and *PIDD1* (pro-apoptotic mediators) and *MDM2* (a p53 feedback regulator). These transcriptional changes suggested that GLU dampens p53-mediated cell cycle checkpoint activation and apoptotic signaling in SP-infected lung mesenchymal cells, potentially contributing to cellular recovery and reduced stress response.

*GLU activated nucleotide sugar metabolism.* GLU intervention significantly upregulated a cluster of core genes involved in nucleotide and amino sugar biosynthesis and nucleotide sugar metabolism (Fig. 5E and F). Key upregulated genes included *GFPT1* and *GFPT2* (glutamine-fructose-6-phosphate transaminases), *UAP1* (UDP-N-acetylglucosamine pyrophosphorylase), *GNE* (UDP-GlcNAc 2-epimerase/ManNAc kinase) and *PGM3* (phosphoacetylglucosamine mutase). Notably, these genes constitute the core enzymatic machinery of the hexosamine biosynthetic pathway (43). *UGP2, GPI, HK1* and *HK3*, which are involved in glucose phosphorylation and UDP-glucose generation (44), were also upregulated. The enhanced expression of *GALE, GMD* and *UXS1*, which catalyze interconversion among UDP-glucose, UDP-galactose, UDP-xylose and GDP-fucose (45), underscored the broad activation of nucleotide sugar biosynthesis. These transcriptional changes suggested that GLU stimulates nucleotide sugar supply and amino sugar metabolism, potentially supporting glycoprotein synthesis and redox homeostasis in lung mesenchymal cells during SP-induced stress.

*FCP suppressed amino acid biosynthesis in SP-infected cells.* FCP treatment (FCP_SP vs. SP) induced significant transcriptional remodeling (Fig. 6A), which involved downregulation of notable pathways, including 'aminoacyl-tRNA biosynthesis', 'biosynthesis of amino acids', 'insulin resistance', 'p53 signaling pathway', 'mTOR signaling pathway' and 'apoptosis (multiple species)'. This phenomenon indicated inhibition of amino acid production, protein synthesis and stress signaling. By contrast, the 'biosynthesis of nucleotide sugars' and 'biosynthesis of amino sugars', as well as 'amino sugar and nucleotide sugar metabolism' pathways were significantly upregulated, reflecting enhanced glycan precursor generation. These changes suggested that FCP attenuates metabolic and apoptotic stress while promoting glycosylation-associated recovery processes in SP-infected lung mesenchymal cells.

In addition, FCP treatment resulted in widespread suppression of both cytoplasmic and mitochondrial aminoacyl-tRNA synthetases in the aminoacyl-tRNA biosynthesis pathway (Fig. 6B). They included *LARS1, YARS1, MARS1, CARS1, AARS1, GARS1, TARS1* and *IARS1*, which are essential for accurate tRNA charging and translational fidelity. Mitochondrial isoforms, such as *LARS2, MARS2, TARS2, PARS2* and *EARS2*, were also downregulated, indicating reduced capacity for mitochondrial protein synthesis. These changes suggested a global attenuation of aminoacylation processes and protein translation following FCP treatment.

In parallel, the biosynthesis of amino acids pathway (Fig. 6C) exhibited coordinated downregulation of multiple metabolic enzymes, including *PHGDH, PSAT1* and *PSPH* (serine synthesis), *SHMT2* (serine-glycine interconversion), ASNS (asparagine synthetase), *BCAT1* (branched-chain amino acid metabolism) and *MAT1A* (methionine activation) (46). Additional suppression of *ALDOB, CPS1, GOT1* and *CTH* further supports reduced amino acid anabolism. These transcriptional changes collectively indicate that FCP inhibits amino acid supply and protein synthesis pathways, potentially contributing to translational downregulation and metabolic reprogramming in SP-infected lung mesenchymal cells.

FCP treatment also downregulated a panel of pro-apoptotic and cell cycle arrest-related genes in the p53 signaling pathway (Fig. 6D). Notably, apoptotic genes, such as *BAX, PMAIP1, CASP8, SIVA1* and *THBS1,* were suppressed, indicating reduced apoptotic signaling (47). In addition, genes associated with cell cycle inhibition, including *CDKN1A (p21), GADD45A, CCNG1, CCNG2, CDK1, CDK4* and *CDK6,*

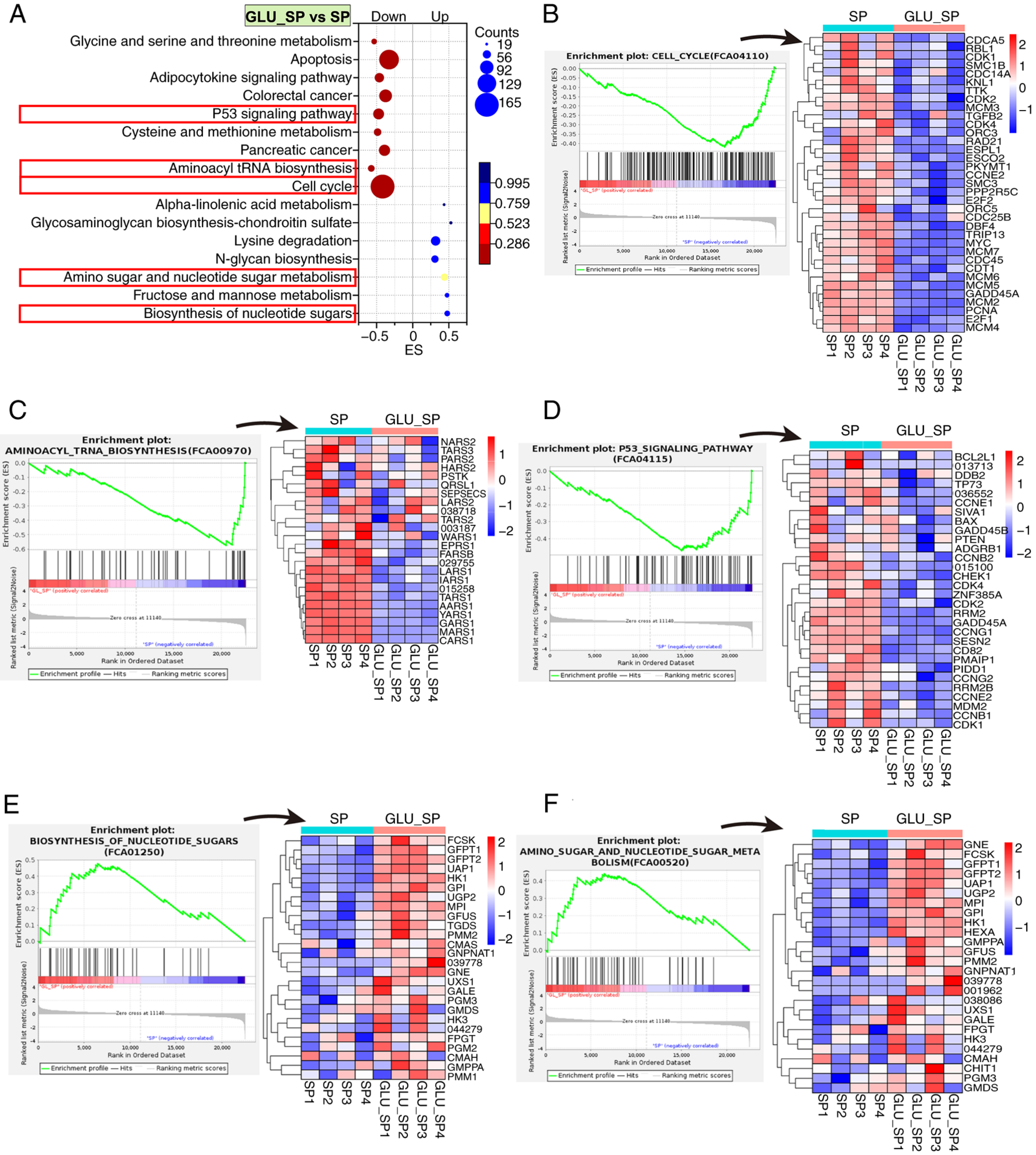

Figure 5. KEGG-based GSEA of transcriptomic changes in FCA-L2 cells following GLU treatment after SP infection. (A) KEGG enrichment bubble plot of pathways significantly altered in the GLU_SP vs. SP group. The x-axis indicates ES, bubble size represents the number of core genes and bubble color corresponds to FDR values. (B-F) GSEA enrichment plots and heatmaps of core genes enriched in representative pathways, including (B) cell cycle, (C) aminoacyl-tRNA biosynthesis, (D) p53 signaling pathway, (E) biosynthesis of nucleotide sugars and (F) amino sugar and nucleotide sugar metabolism. Heatmaps display Z-score normalized expression levels (n=4 per group). KEGG, Kyoto Encyclopedia of Genes and Genomes; GSEA, gene set enrichment analysis; GLU, glutamine; SP, *Streptococcus pneumoniae;* NC, negative control; ES, enrichment score; FDR, false discovery rate.

were also downregulated, suggesting partial release from p53-induced cell cycle arrest (47). By contrast, FCP treatment upregulated *CASP3* (a central effector caspase), *BCL2* (anti-apoptotic), *CCND3* (G1/S cyclin) and stress response mediators, such as *GADD45B*, *SESN1* and *SESN3* (47). This phenomenon suggested a shift toward adaptive stress recovery rather than p53-mediated apoptosis. These changes collectively suggest that FCP inhibits excessive p53-driven cytotoxicity while promoting moderate survival and stress adaptation in SP-infected lung mesenchymal cells.

*FCP activated nucleotide sugar metabolism*. FCP treatment significantly upregulated a set of core genes involved in amino and nucleotide sugar metabolism and nucleotide

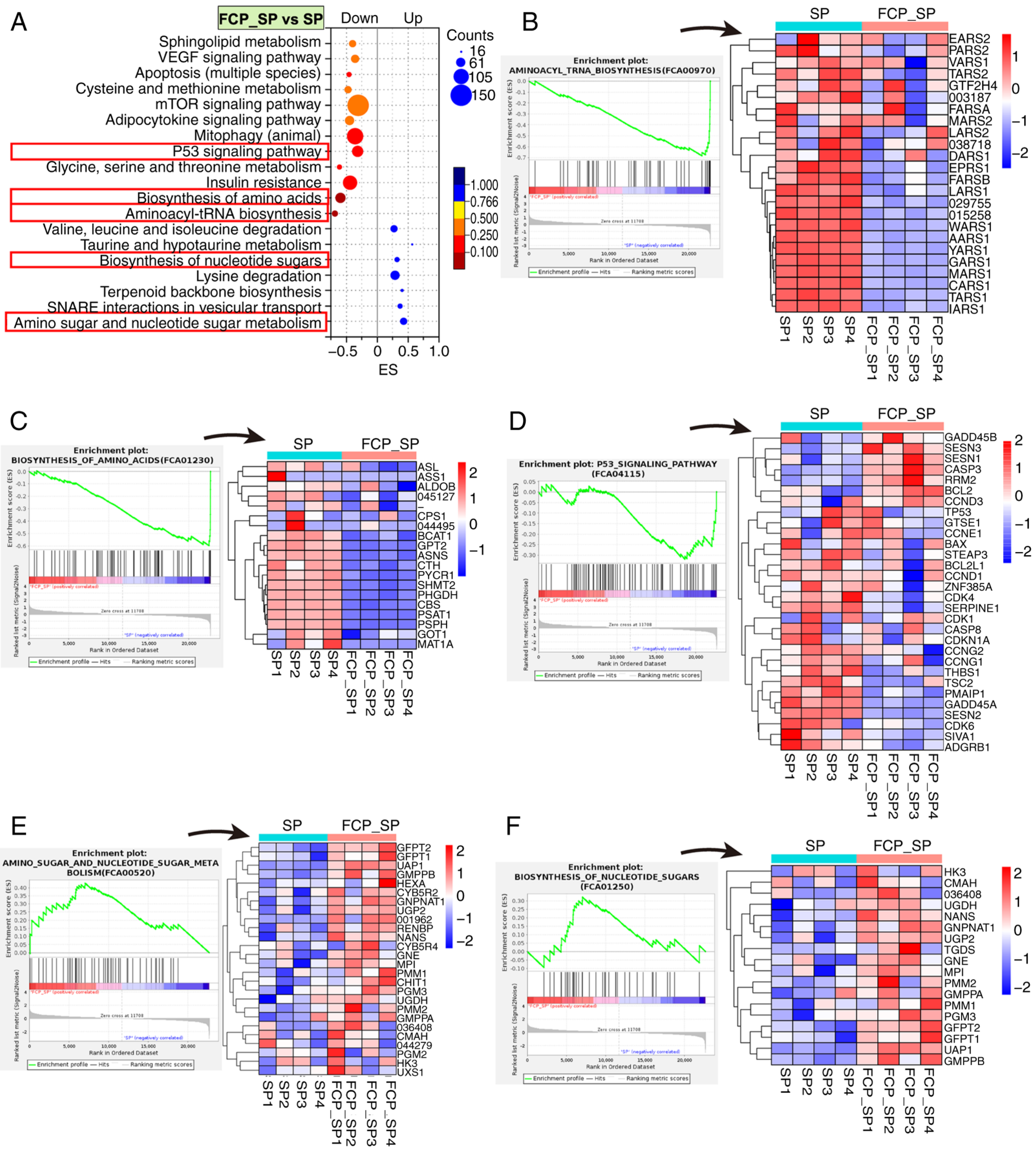

Figure 6. KEGG-based GSEA of transcriptomic changes in FCA-L2 cells following FCP treatment after SP infection. (A) KEGG enrichment bubble plot showing pathways significantly regulated in the FCP_SP vs. SP group. The x-axis represents ES, bubble size indicates the number of enriched genes and color corresponds to the FDR. (B-F) GSEA enrichment plots and heatmaps of core genes in selected pathways, including (B) aminoacyl-tRNA biosynthesis, (C) biosynthesis of amino acids, (D) p53 signaling pathway, (E) amino sugar and nucleotide sugar metabolism and (F) biosynthesis of nucleotide sugars. Heatmaps show Z-score-normalized gene expression (n=4 per group). KEGG, Kyoto Encyclopedia of Genes and Genomes; GSEA, gene set enrichment analysis; FCP, fish collagen peptides; SP, *Streptococcus pneumoniae;* NC, negative control; ES, enrichment score; FDR, false discovery rate.

sugar biosynthesis, indicating enhanced flux through hexosamine and UDP-sugar pathways (Fig. 6E and F). Notably, *GFPT1*, *GFPT* and *UAP1*, which encode the rate-limiting enzymes for hexosamine biosynthesis, were strongly induced, suggesting elevated UDP-GlcNAc production (48). Concurrent upregulation of *GNE*, *MPI*, *PMM1*, *PMM2*, *GMPPA*, *GMPPB*, *PGM3* and *UGP2* further supported enhanced biosynthesis of diverse nucleotide sugars, including UDP-GalNAc, GDP-mannose and UDP-glucose (48). Genes essential for sialic acid and GlcNAc-6-phosphate conversion, such as *NANS* and *GNPNAT1*, were also elevated (49). These transcriptional changes indicated that FCP stimulates nucleotide sugar biosynthetic networks in SP-infected lung mesenchymal cells, potentially facilitating glycosylation, membrane repair and metabolic compensation under SP-induced stress.

*Metabolomic alterations*. PCA analysis of metabolomic profiles (Fig. 7A) revealed clear separation among SP, NC, GLU and FCP groups, indicating distinct metabolic states. Notably, numerous metabolites were significantly altered in each comparison (Fig. 7B). SP infection induced significant elevation of lipids and lipid-like molecules, including MG(0:0/i-13:0/0:0), MG(0:0/i-15:0/0:0) and palmitoylcarnitine. By contrast, several amino acids and related compounds, such as proline-arginine-leucine and tyrosine-glutamine-phenylalanine, were strongly downregulated (Table SIII).

GLU intervention (GLU_SP vs. SP; Table SIV) resulted in significant upregulation of metabolites such as isoamyl isothiocyanate, lauroyl diethanolamide and 4,5-dihydroxyhexanoic acid. Numerous amino acids and peptides, including arginine-leucine-isoleucine, l-lysyl-l-lysyl-l-lysine and tyrosine-glutamine-phenylalanine and small oligopeptides, such as Ala-Leu-Leu-Thr, were also significantly upregulated. By contrast, a broad range of lipids, including lysophosphatidylcholine [22:2(13Z,16Z)/0:0] and monoacylglycerol [MG(0:0/i-13:0/0:0)], were significantly decreased.

The prominent upregulated metabolites in the FCP intervention group (FCP_SP vs. SP; Table SV) included cycloart-23-ene-3β,25-diol, ethyl linoleate and prolylproline, suggesting enhanced lipid signaling and peptide metabolism. Conversely, glutamylleucylarginine, N-benzoyl-D-arginine, PS (20:4-OH (12S)/14:1) and homaxisterol B1 were among the most significantly downregulated lipids and sterols.

*Metabolite GSEA analysis*. SP infection significantly downregulated 'glycerophospholipid metabolism', 'choline metabolism in cancer' and 'arginine and proline metabolism' (Fig. 7C), suggesting disrupted membrane lipid turnover and amino acid-derived signaling (50,51). GLU treatment significantly activated 'purine metabolism' and 'ABC transporters' but did not affect 'choline metabolism in cancer', 'glycerophospholipid metabolism' and 'biosynthesis of unsaturated fatty acids'. By contrast, FCP treatment upregulated 'choline metabolism in cancer,' 'glycerophospholipid metabolism' and 'biosynthesis of amino acids' and 'biosynthesis of unsaturated fatty acids'.

Notably, within the 'choline metabolism in cancer' pathway (Fig. 7D), a set of SP-affected metabolites was identified, including LysoPC (22:6/0:0), LysoPC (18:3/0:0), LysoPC (22:5/0:0) and LysoPC (20:4/0:0) (Fig. 7D). The presence of these polyunsaturated lysophosphatidylcholines denoted SP-induced membrane remodeling and lipid depletion.

GLU treatment significantly elevated purine metabolites (Fig. 7E), such as cyclic GMP, GTP, GMP, xanthosine, xanthine, adenosine triphosphate, adenylosuccinic acid and dADP, which reflect enhanced nucleotide turnover and energy metabolism under SP infection stress (52). By contrast, FCP treatment increased biosynthesis of amino acids (Fig. 7F) by upregulating sedoheptulose 7-phosphate, S-adenosylhomocysteine, argininosuccinic acid, L-histidine, L-ornithine, L-glutamine and N6-(L-1,3-dicarboxypropyl)-L-lysine, which denoted strengthened amino acid regeneration and one-carbon metabolism. In addition, FCP treatment enhanced biosynthesis of unsaturated fatty acids, elevating nervonic acid, cis-11-eicosenoic acid, EPA, DHA, alpha-linolenic acid and arachidonic acid. This phenomenon suggested restored membrane lipid homeostasis and anti-inflammatory lipid mediator production.

*Integrated pathway analysis of transcriptome and metabolome*. The number of differential genes and metabolites varied across comparisons, with SP infection causing the most extensive changes (Fig. 8A). Integrated enrichment analysis revealed that SP infection significantly affected 'biosynthesis of amino acids', 'carbon metabolism', 'endocytosis' and the 'Rap1 signaling pathway' (Fig. 8B). Notably, genes involved in endocytic trafficking, including RAB11B, were strongly upregulated (Fig. 4C), while guanosine triphosphate (GTP), which is a crucial metabolite, was significantly reduced (Table SIII). This phenomenon reflected enhanced membrane recycling activity driven by GTP-dependent GTPases under infection stress, accompanied by energy depletion and disrupted purine metabolism, resulting in intracellular GTP shortage despite increased demand (53).

*GLU enhanced nitrogen assimilation and amino acid synthesis under SP infection*. Integrated KEGG analysis revealed that GLU treatment significantly modulated 'aminoacyl-tRNA biosynthesis', 'biosynthesis of amino acids', 'phospholipase D signaling pathway', 'purine metabolism' and 'choline metabolism in cancer' (Fig. 8C); the 'biosynthesis of amino acids' pathway was prominently activated. The key upregulated genes included *ALDH18A1* ($\Delta^1$-pyrroline-5-carboxylate synthase, proline biosynthesis), *IDH1* (isocitrate dehydrogenase, TCA cycle and glutamate conversion), *PYCR3* (pyrroline-5-carboxylate reductase, proline biosynthesis), *ENO1*/*ENO3, PFKL, ALDOA* and *GAPDH* (glycolytic enzymes) and *ACO2* (aconitase, TCA cycle) (Table SVI). Metabolomic data further confirmed significant elevation of pathway-relevant metabolites, including L-histidine, L-lysine, L-proline, L-ornithine, S-adenosylmethionine, argininosuccinic acid, L-arginine, L-methionine, L-phenylalanine, L-asparagine, histaminol and citrate (Table SVI). This phenomenon supported the transcriptional activation of amino acid biosynthetic machinery.

*FCP intervention enhanced amino and nucleotide sugar metabolism*. FCP treatment significantly regulated multiple metabolic pathways, including 'amino sugar and nucleotide sugar metabolism', 'carbon metabolism', 'steroid biosynthesis' and 'pathways in cancer' (Fig. 8D); among them, 'amino sugar and nucleotide sugar metabolism' was prominently activated. Metabolomic analysis revealed an increase in galactose 1-phosphate and a reduction in cyclic N-acetyl-D-mannosamine, which indicated altered hexosamine flux (Table SVI). Transcriptomic data revealed robust upregulation of *GFPT1, GFPT2* and *UAP1*, which encode key rate-limiting enzymes in UDP-GlcNAc biosynthesis (Table SVI). Additionally, *GNE, MPI, PMM1, PMM2, GMPPA, GMPPB, PGM3* and *UGP2* were elevated (Table SVI), supporting enhanced production of multiple nucleotide sugars, including UDP-GalNAc, GDP-mannose and UDP-glucose. These changes suggested that FCP promotes nucleotide sugar biosynthesis.

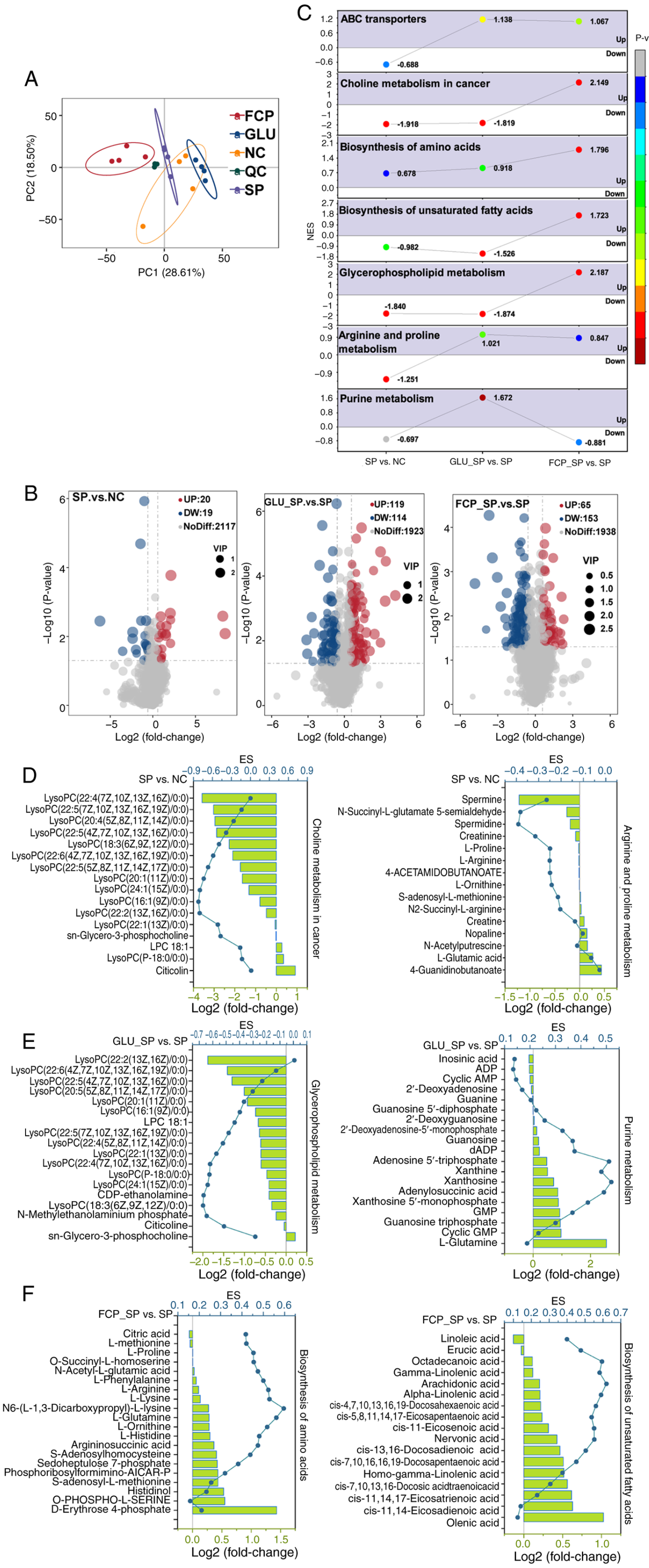

Figure 7. Untargeted metabolomic profiling and pathway enrichment analysis in FCA-L2 cells. (A) PC analysis score plot showing sample distribution across treatment groups. (B) Volcano plots of differential metabolites in SP vs. NC, GLU_SP vs. SP and FCP_SP vs. SP comparisons. Significantly changed metabolites are colored by fold change and significance threshold. (C) Metabolite set enrichment analysis comparing SP vs. NC, GLU_SP vs. SP and FCP_SP vs. SP. The x-axis represents comparison groups; the y-axis lists enriched Kyoto Encyclopedia of Genes and Genomes pathways; NES>0 indicates pathway upregulation. (D) Enrichment plots of downregulated metabolites in glycerophospholipid metabolism and arginine and proline metabolism (SP vs. NC). (E) Enrichment plots showing downregulation of glycerophospholipid metabolism and upregulation of purine metabolism (GLU_SP vs. SP). (F) Enrichment plots showing upregulated metabolites in biosynthesis of amino acids and biosynthesis of unsaturated fatty acids (FCP_SP vs. SP). PC, principal component; GLU, glutamine; FCP, fish collagen peptides; SP, *Streptococcus pneumoniae;* NC, negative control; QC, quality control; NES, normalized enrichment score.

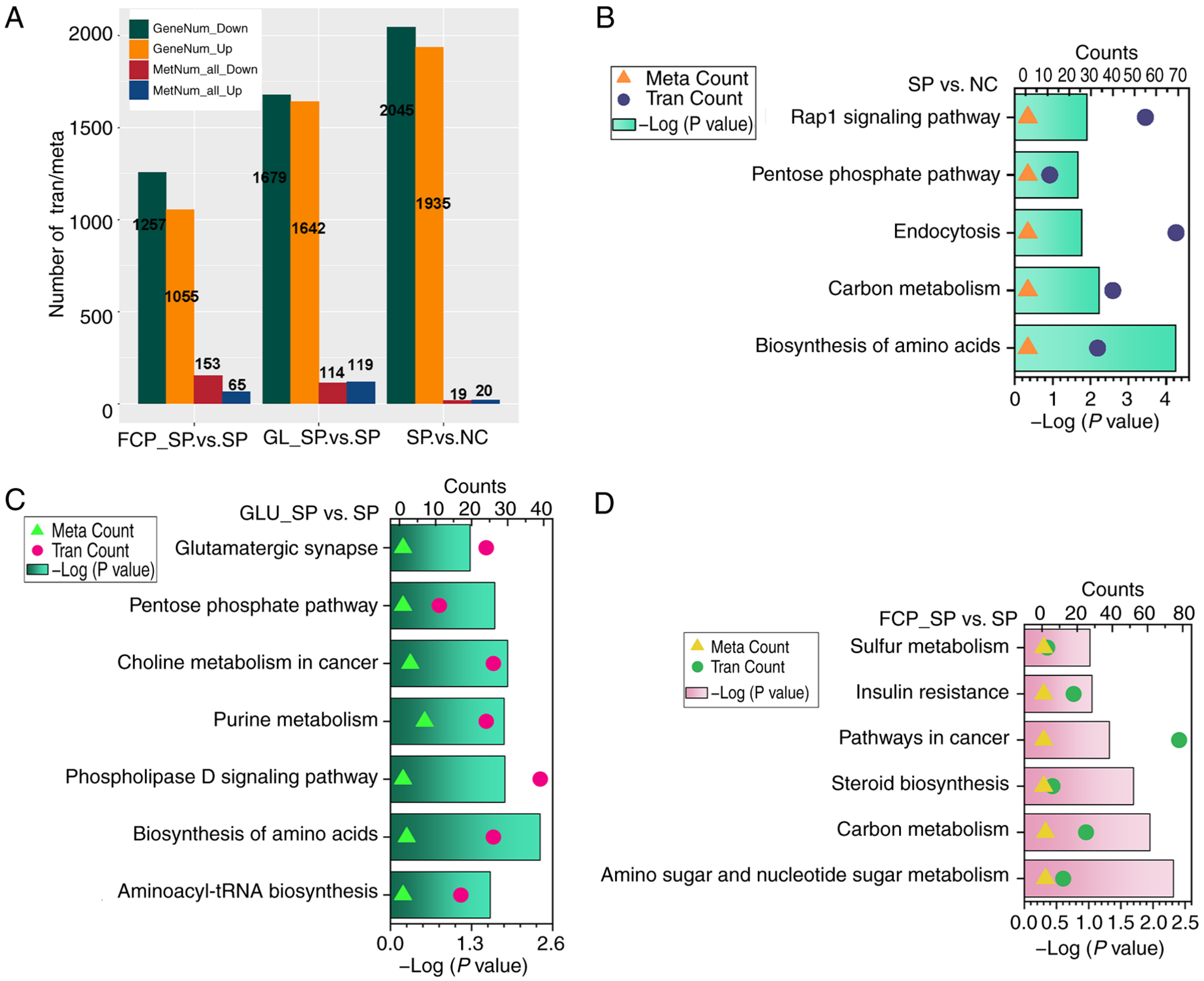

Figure 8. Integrated transcriptomic and metabolomic analysis of FCA-L2 cells. (A) Bar plot showing the number of differentially expressed genes and differential metabolites in SP vs. NC, GLU_SP vs. SP and FCP_SP vs. SP comparisons. (B-D) Joint Kyoto Encyclopedia of Genes and Genomes enrichment analysis of transcriptomic and metabolomic datasets using hypergeometric testing. Bubble plots show commonly enriched pathways in (B) SP vs. NC, (C) GLU_SP vs. SP and (D) FCP_SP vs. SP groups. The x-axis represents-log(P-value) based on Fisher's exact test. Bubble size indicates total number of molecules mapped to the pathway and shape indicates omics source. GLU, glutamine; FCP, fish collagen peptides; SP, *Streptococcus pneumoniae;* NC, negative control; Tran, transcriptomics; meta, metabolomics.

*Correlation analysis between key genes and metabolites in the GLU_SP vs. SP group*. Pearson correlation analysis between key genes and metabolites derived from the core pathways identified by joint KEGG enrichment analysis was performed to characterize the functional coupling between transcriptional changes and metabolite remodeling induced by GLU supplementation (Fig. 9A). Notably, a structured correlation pattern was observed in the GLU_SP vs. SP group. Genes belonging to the serine biosynthesis and one-carbon metabolism axis, which included *PHGDH*, *PSAT1*, *PSPH*, *SHMT2* and *ASNS*, exhibited consistently strong negative correlations with GLU and multiple peptide-related metabolites (most |r|>0.95). In particular, L-glutamine and a panel of di- and tripeptides, including Ala-Leu-Leu-Thr, Gly-Phe-Val, Leu-Val-Ser and Ser-Leu-Ile, clustered tightly and showed inverse correlations with the *PHGDH-PSAT1-PSPH-SHMT2* gene module. This pattern indicated that GLU treatment enhanced the utilization of nitrogen substrates and peptide-derived amino acids, rather than their accumulation, suggesting accelerated amino acid flux into biosynthetic pathways.

In parallel, a distinct metabolite cluster composed of lysophospholipids (LysoPC, LysoPG), monoacylglycerols, phosphatidylcholine species, acylcarnitines and unsaturated fatty acid derivatives displayed strong positive correlations with the *PHGDH-PSAT1-PSPH-SHMT2* gene module. The coherence of these lipid-associated metabolites in both hierarchical clustering and correlation direction suggested that GLU treatment facilitates concerted remodeling of membrane lipid composition and mitochondrial lipid metabolism.

Notably, genes involved in transamination (*GPT2* and *BCAT1*), proline biosynthesis (*ALDH18A1* and *PYCR1*) and sulfur-containing amino acid metabolism (*CBS* and *CTH*) exhibited correlation patterns consistent with the central serine-one-carbon module. These genes collectively formed a connected network regulating amino acid interconversion, nitrogen redistribution and redox balance, supporting

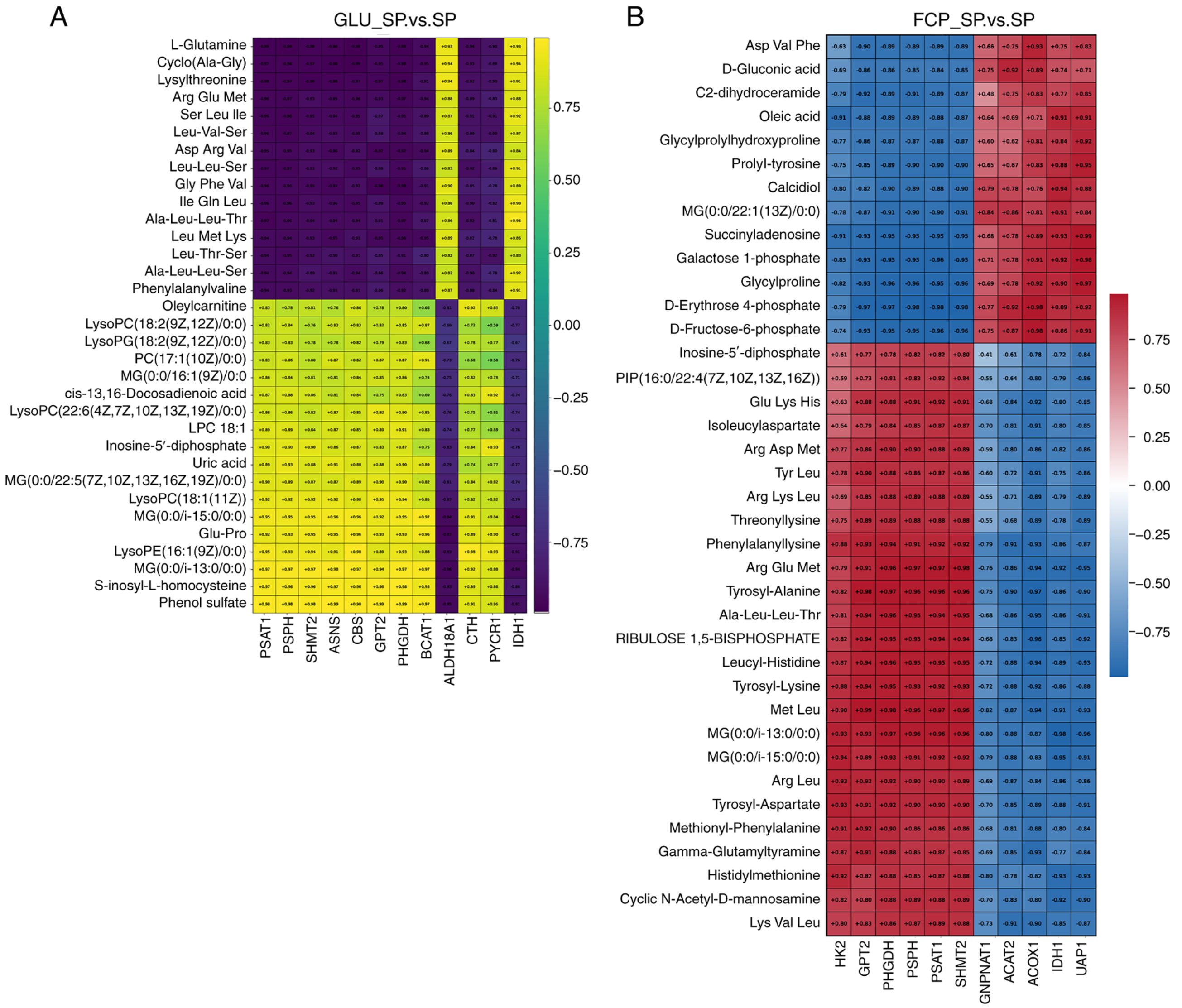

Figure 9. Correlation analysis between key genes and metabolites derived from joint transcriptomic-metabolomic enrichment. (A) Pearson correlation heatmap showing associations between differentially expressed genes and differential metabolites in the GLU_SP vs. SP group. (B) Pearson correlation heatmap showing associations between differentially expressed genes and differential metabolites in the FCP_SP vs. SP group. Pearson correlation coefficients were calculated to evaluate the consistency of variation trends between gene expression and metabolite abundance. Positive correlations indicate coordinated changes, whereas negative correlations indicate inverse regulatory relationships. Each grid is annotated with the corresponding correlation coefficient. Hierarchical clustering was applied to both genes and metabolites to identify functional association modules. GLU, glutamine; FCP, fish collagen peptides; SP, *Streptococcus pneumoniae*

the presence of a coordinated amino acid metabolic reprogramming network in the GLU-treated cells.

The correlation architecture demonstrated that GLU treatment induces a directional metabolic reorganization characterized by active nitrogen consumption, enhanced amino acid biosynthetic flux and coordinated lipid metabolic adaptation rather than simply elevating metabolite abundance under SP infection (Fig. 9).

*Correlation analysis between key genes and metabolites in the FCP_SP vs. SP group.* Pearson correlation analysis between differential metabolites and key genes derived from the core pathways identified by joint KEGG enrichment analysis was performed to characterize the association between transcriptional alterations and metabolic changes induced by FCP treatment (Fig. 9B). Genes involved in the serine biosynthesis and one-carbon metabolism pathway (*PHGDH, PSAT1, PSPH* and *SHMT2*) exhibited notably consistent correlation directions across a broad spectrum of metabolites. Notably, they had strong positive correlations with multiple peptide-related metabolites, including Ala-Leu-Leu-Thr, Met-Leu, Arg-Glu-Met, Leucyl-Histidine and Lys-Val-Leu. By contrast, they were strongly negatively correlated with several carbohydrate-related intermediates, such as D-erythrose-4-phosphate, D-fructose-6-phosphate and galactose-1-phosphate.

A similar correlation profile was observed for *GPT2*, which displayed positive correlations with the majority of peptide metabolites, including Met-Leu (and Ala-Leu-Leu-Thr, but inverse correlations with sugar phosphate intermediates, such as D-erythrose-4-phosphate and D-fructose-6-phosphate. This coherence suggested that genes involved in amino acid interconversion were tightly coupled to peptide turnover and central carbon metabolism under FCP treatment.

Notably, genes involved in amino and nucleotide sugar metabolism, including *UAP1* and *GNPNAT1*, had distinct associations with carbohydrate-related metabolites. *UAP1* exhibited strong positive correlations with galactose-1-phosphate, D-erythrose-4-phosphate and D-fructose-6-phosphate. However, it exhibited negative correlations with multiple peptide metabolites (such as Met-Leu; Ala-Leu-Leu-Thr). These findings were consistent with the transcriptional activation of the amino and nucleotide sugar biosynthetic pathway in joint KEGG enrichment.

In addition, genes associated with central carbon and lipid metabolism, including *IDH1*, *ACAT2* and *ACOX1*, were significantly and positively correlated with both carbohydrate intermediates (e.g., D-fructose-6-phosphate) and lipid-associated metabolites. These metabolites included monoacylglycerols, oleic acid and C2-dihydroceramide, underscoring the coordinated remodeling of energy and lipid metabolism in response to FCP treatment.

## Discussion

The present study investigated the molecular responses of feline pulmonary interstitial cells (FCA-L2) following SP infection and subsequent antibiotic treatment. Integrated transcriptomic and metabolomic analyses revealed persistent cell injury, sustained inflammatory activation and significant remodeling of lipid metabolism and intracellular trafficking, which provide mechanistic insights into post-infection pathophysiology.

Notably, there was significant LDH release, elevated IL-1β, TNF-α and IL-8 expression, increased MDA levels, and disruption of junction proteins after 18 h despite antibiotic administration at 4 h post-infection. These findings indicate that bacterial clearance alone is insufficient to prevent secondary damage, supporting the presence of a post-infectious inflammatory syndrome. Notably, this phenomenon is consistent with clinical reports in SP-related pneumonia, where excessive immune activation and residual bacterial components, such as pneumolysin and cell wall fragments, continue to trigger damage-associated signaling even after pathogen eradication (54,55). The reduction in junction proteins suggests compromised barrier integrity due to cytokine-mediated cytoskeletal rearrangement and oxidative injury. These observations reflect crucial features of infection-associated acute lung injury, underscoring the need for adjunctive interventions beyond antibiotics (56).

Notably, SP infection induced transcriptional and metabolic remodeling of glycerophospholipid metabolism by significantly upregulating key enzymes involved in *de novo* phospholipid synthesis and hydrolysis, including *GPAT3, AGPAT1, LPIN1* and *PLA2G6*, which enhance membrane lipid turnover (57,58). Metabolomic data confirmed enrichment of the glycerophospholipid metabolism pathway. In particular, there were reductions in multiple lysophosphatidylcholine (LysoPC) species and increased levels of CDP-ethanolamine and citicoline, which mediate PC biosynthesis. These findings indicate active membrane remodeling, potentially driven by stress and repair demands. Notably, the significant depletion of multiple polyunsaturated LysoPC species, including LysoPC 22:6/0:0, LysoPC 22:5/0:0 and LysoPC 20:4/0:0 potentially compromises membrane stability and increases membrane fragility (59). This finding is consistent with the elevated LDH release and disruption of tight junction proteins observed in SP-infected cells. LysoPC depletion may result from increased utilization for membrane repair or altered PLA2 activity (60). Elevated citicoline levels support compensatory PC synthesis to maintain membrane integrity; however, excessive phospholipid turnover may paradoxically destabilize membrane architecture under sustained stress conditions. Alterations in phospholipids affect membrane curvature, fluidity and raft formation, which modulate host-pathogen interactions (61,62). In the present study, enhanced membrane remodeling potentially facilitates SP internalization or intracellular persistence by disrupting immune receptor localization and amplifying inflammatory signaling through lipid-derived mediators. Enhanced membrane turnover may promote SP internalization or intracellular survival by disrupting immune receptor localization. Excessive lipid remodeling may also amplify inflammation via lipid mediators and destabilization of membrane signaling platforms.

SP infection also activated endocytosis-related pathways, further supporting membrane remodeling and persistent intracellular stress (62). Transcriptomic upregulation of *RAB11B, RAB11FIP3, AP2A1* and *DNM1* indicated the activation of recycling endosomes and clathrin-mediated endocytosis (63). Metabolomic analysis revealed reduced intracellular GTP levels, suggesting high consumption during vesicle trafficking, which is energetically costly and may impose a substantial metabolic burden on infected cells (64). This finding was evidenced by the increased oxidative stress and apoptosis observed in SP-treated cells. Upregulated RAB11 signaling may enhance receptor recycling, antigen processing and cytokine transport (65). The enhanced receptor recycling capacity may contribute to prolonged surface availability of cytokine receptors and pattern-recognition receptors, thereby reinforcing inflammatory signaling. This phenomenon was observed in the present study, as evidenced by the elevated levels of IL-1β, TNF-α and IL-8. Notably, SP can exploit this machinery to evade immune surveillance or promote intracellular persistence. These alterations are closely linked to immune modulation through potential activation of endosomal toll-like receptors (TLRs), including *TLR3* and *TLR9*, leading to cytokine activation (61). Moreover, excessive endosomal flux may overload the endosome-lysosome system and impair autophagic homeostasis, leading to increased cellular stress and apoptotic vulnerability (66,67). This mechanism provides a plausible explanation for the elevated apoptosis and cytotoxicity observed in the present study following SP infection.

In the present study, GLU and FCP treatments significantly alleviated SP-induced cellular injury and inflammation. GLU and FCP reduced LDH release, suppressed pro-inflammatory cytokine expression, restored tight junction proteins and slowed apoptosis and cell death. They also enhanced antioxidant capacity, which highlighted their dual cytoprotective effect mediated by metabolic support and anti-inflammatory modulation.

GLU treatment downregulated multiple cell cycle regulators, including *CDK1, CDK2, CCNE2* and *MCM* family genes, and suppressed aminoacyl-tRNA synthetases, such as *EPRS1* and *LARS1* (68,69). However, the amino acid biosynthesis pathway was significantly upregulated at both transcriptomic and metabolomic levels. Key upregulated genes included *ALDH18A1, PYCR3, IDH1, ACO2, ENO1, ENO3, PFKL, ALDOA* and *GAPDH*, translating to activation of proline biosynthesis, glycolysis and the TCA cycle (69). Metabolomic profiling confirmed increased levels of L-proline, L-lysine, L-ornithine, S-adenosylmethionine, argininosuccinate, L-arginine and L-histidine. This difference suggests that GLU induces the preferential accumulation of free amino acids for stress defense, rather than protein synthesis. Aminoacyl-tRNA synthetases are essential components of the translational machinery; downregulation indicates a deliberate reduction in protein synthesis, potentially to prevent the accumulation of misfolded proteins and mitigate endoplasmic reticulum stress under infection-induced damage (70). In parallel, upregulated amino acid biosynthesis supports antioxidant defenses and energy metabolism. Notably, this metabolic shift directly correlates with the decreased apoptosis and oxidative stress observed in the present functional assays following GLU treatment. For example, upregulation of ALDH18A1 and PYCR3 promotes proline synthesis, contributing to redox buffering and mitochondrial protection (71,72). IDH1 and ACO2 facilitate NADPH production and maintain TCA cycle integrity. Elevated glycolytic enzyme expression suggests increased glycolytic flux to support biosynthetic demands and ATP supply (14). The enhancement of NADPH-dependent redox buffering and ATP-generating pathways provides a mechanistic explanation for the improved antioxidant capacity (SOD, GPX, T-AOC/TOS) and the preservation of cell viability observed in functional assays.

FCP treatment significantly activated amino and nucleotide sugar metabolism. Transcriptomic analysis revealed upregulation of *GFPT1, GFPT2* and *UAP1*, indicating increased synthesis of UDP-N-acetylglucosamine (UDP-GlcNAc) (73). Upregulation of *GNE, MPI, PMM1, PMM2, GMPPA, GMPPB, PGM3* and *UGP2* suggested enhanced biosynthesis of multiple nucleotide sugars, including UDP-GalNAc, GDP-mannose and UDP-glucose. Notably, genes involved in sialic acid and GlcNAc-6-phosphate production (*NANS* and *GNPNAT1*) were also elevated (74). These transcriptomic changes were consistent with the metabolomic data, which exhibited increased galactose 1-phosphate and decreased cyclic N-acetyl-D-mannosamine. This response is closely associated with the pathogenic mechanism of SP; SP expresses a range of glycosidases, such as neuraminidase (NanA), β-galactosidase and β-N-acetylglucosaminidase, which cleave host glycoproteins and glycolipids, thereby exposing hidden epithelial receptors to facilitate bacterial adhesion (54,55,61,62). NanA also degrades mucins, thereby reducing mucosal viscosity and weakening the protective barrier (61). The activation of amino sugar and nucleotide sugar metabolism by FCP potentially restored glycosylation of membrane proteins and the structural integrity of the glycocalyx, thereby counteracting bacterial deglycosylation and promoting membrane repair. Mechanistically, FCP-derived peptides potentially trigger the activation of nucleotide sugar biosynthesis in a multifactorial manner. Small peptides can be transported into cells through proton-coupled oligopeptide transporters, including PEPT1 (*SLC15A1*) and PEPT2 (*SLC15A2*), which mediate the uptake of di-/tripeptides and certain peptide-like substrates (75-77). Peptides and amino acids generated by intracellular peptidases upon entry of the small peptides may enhance cellular nitrogen availability and one-carbon metabolism, thereby supporting the biosynthetic demand required for UDP-sugar production (78,79). In parallel, peptide uptake and/or amino acid sensing could activate nutrient-responsive signaling, such as mTOR/ATF4-related adaptive programs (80,81), which coordinate anabolic pathways under stress and may contribute to the observed upregulation of GFPT1/2 and UAP1. Functionally, restoration of membrane glycosylation stabilizes surface proteins and junctional complexes. This phenomenon was exemplified in the present study by the recovery of tight junction protein expression and reduced LDH leakage following FCP treatment. FCP also enhanced amino acid and polyunsaturated fatty acid (PUFA) metabolism. Metabolomic analysis in the present study revealed elevated levels of key intermediates in amino acid biosynthesis, including L-histidine, L-arginine, L-glutamine, L-proline, L-lysine and S-adenosylmethionine. Glycolytic and pentose phosphate pathway intermediates, such as sedoheptulose 7-phosphate and erythrose 4-phosphate, were also elevated. In parallel, there was an increase in the levels of multiple long-chain PUFAs, including alpha-linolenic acid, eicosapentaenoic acid, docosahexaenoic acid and nervonic acid. Upregulation of amino acid and PUFA metabolism functionally synergizes with nucleotide sugar biosynthesis. Specifically, the accumulation of proline and other amino acids provides essential precursors for cellular repair and redox homeostasis, while the elevated long-chain PUFAs (e.g., EPA and DHA) act as anti-inflammatory mediators to counteract SP-induced cytokine production and membrane oxidative damage (71,72,82-84). The coordinated metabolic reprogramming provides a mechanistic explanation for the observed attenuation of inflammatory cytokine production, reduced oxidative stress and improved cell survival following FCP intervention. The coordinated metabolic programs contributed to membrane structure repair, glycan renewal and cellular recovery from infection-induced stress.

Alveolar epithelial cells are the primary sites of SP adhesion and barrier disruption during the acute phase of infection (85-87). However, increasing evidence indicates that the resolution of lung injury involves active participation of pulmonary interstitial fibroblast populations during the post-infectious repair phase, partly through paracrine signaling that supports alveolar and parenchymal regeneration (88-90). Mesenchymal cells contribute to tissue recovery by regulating ECM remodeling, resolving inflammatory responses and re-establishing a microenvironment conducive to epithelial regeneration following bacterial clearance (25). In this context, mesenchymal cells function as key coordinators of lung repair rather than direct targets of bacterial invasion. The use of mesenchymal cells in the present study is thus particularly relevant for investigating reparative mechanisms that operate after infection-induced damage, rather than the initial host-pathogen interaction. The protective effects seen in mesenchymal cells in the present study may influence epithelial recovery *in vivo*. Mesenchymal cells influence epithelial repair through paracrine signaling, including the secretion of growth factors, cytokines and matrix-regulating molecules that promote epithelial cell proliferation, migration and restoration of barrier integrity (88-93). The attenuation of inflammation and oxidative stress, along with the preservation of junction-associated proteins observed in the present study, suggests that the intervention may contribute to the formation of a reparative microenvironment that indirectly supports epithelial regeneration following pneumococcal injury.

Notably, the concentrations of GLU (40 mM) and FCP (500 $\mu$g/ml) were determined via standardized *in vitro* screenings to achieve an optimal balance between non-cytotoxicity and maximal reparative efficacy. These pharmacological doses are independent of systemic physiological plasma benchmarks because the metabolic and structural requirements for cellular repair in an *in vitro* environment represent a biological dimension distinct from systemic homeostasis. Nevertheless, these doses provide a theoretical foundation for targeted clinical strategies, such as localized pulmonary nebulization and inhalation therapy. However, it must be acknowledged that the current *in vitro* monoculture model lacks the inherent complexity of the lung microenvironment, which involves dynamic interactions between various immune cells, including alveolar macrophages and neutrophils and the three-dimensional ECM. These factors could markedly influence the observed reparative effects in an *in vivo* setting. For instance, GLU is a critical metabolic fuel for macrophages (52). Its supplementation could support fibroblast-mediated repair and modulate macrophage polarization toward a pro-resolving M2 phenotype, potentially creating a synergistic effect that accelerates tissue clearance and healing (94,95). Similarly, FCP may interact with the native ECM architecture to further enhance structural integrity (19). The simplified model established in the present study essentially isolates and delineates the specific metabolic and transcriptomic reprogramming within pulmonary interstitial fibroblasts. However, future studies employing 3D organoid models or *in vivo* animal infection trials should be conducted to extensively capture the multicellular synergy during the post-antibiotic lung recovery phase.

Despite the numerous insightful outputs of the present study, it was limited by several factors. The use of a mesenchymal cell model did not directly capture the initial epithelial-pathogen interactions that occurred during SP infection. The findings of the present study provide mechanistic insights into stromal-mediated reparative responses following infection-induced injury. However, the intercellular crosstalk and epithelial-specific responses under infectious conditions should be validated through future studies using epithelial cells or mesenchymal-epithelial co-culture systems. In addition, a DOX-only group was not included in the transcriptomic and metabolomic analyses. The experimental contrasts were designed to characterize molecular alterations associated with the post-infectious, post-antibiotic state (SP + Dox), and their modulation by nutritional interventions. Future studies incorporating a Dox-only control will be valuable for fully disentangling antibiotic-associated molecular effects from post-infectious host responses.

In conclusion, SP induced sustained cell injury and inflammation, accompanied by lipid remodeling, endocytic activation and metabolic imbalance in FCA-L2 cells. However, SP-induced damage was significantly alleviated by both GLU and FCP through synergistic metabolic and anti-inflammatory effects. GLU reprogrammed amino acid metabolism and redox homeostasis, whereas FCP restored glycosylation and membrane integrity by enhancing UDP-sugar, amino acid and PUFA metabolism. These results of the present study underscore the importance of targeting host metabolic and structural pathways to mitigate SP-related lung injury. They also support the development of adjunctive therapies beyond antibiotics.

## Acknowledgements

The authors would like to acknowledge the Global Pet Cell Resource Center PETCC for providing the cells and culture technology support.

## Funding

No funding was received.

## Availability of data and materials

The raw RNA-sequencing data have been deposited in the NCBI Sequence Read Archive (SRA) under BioProject accession number PRJNA1416572. The raw metabolomics data have been deposited in the Figshare open-access repository and are publicly available under the DOI 10.6084/m9.figshare.31267111 (https://doi.org/10.6084/m9.figshare.31267111). All other data generated in the present study may be requested from the corresponding author.

## Authors' contributions

HB contributed to the investigation, methodology design, validation of experiments and drafting of the original manuscript. TL contributed to data curation, formal analysis, software processing and data visualization. HW contributed to the investigation and validation. HJ contributed to conceptualization, project administration and provision of resources. YL contributed to resources and conceptualization of the study. ZW contributed to conceptualization, supervision and critical review and editing of the manuscript. All authors have read and approved the final version of the manuscript. HB and ZW confirm the authenticity of all the raw data.

## Ethics approval and consent to participate

Not applicable.

## Patient consent for publication

Not applicable.

## Competing interests

The authors declare that they have no competing interests.

## References

1. Li Y, Jiang Y, Zhang H, Zhang J, Ma J, Yang Z, Qiu M and Wang J: Research on acute lung injury inflammatory network. Int J Clin Pharmacol Ther 61: 394-403, 2023.
2. Lanks CW, Musani AI and Hsia DW: Community-acquired pneumonia and hospital-acquired pneumonia. Med Clin North Am 103: 487-501, 2019.
3. de Benedictis FM, Kerem E, Chang AB, Colin AA, Zar HJ and Bush A: Complicated pneumonia in children. Lancet 396: 786-798, 2020.
4. Liu YN, Zhang YF, Xu Q, Qiu Y, Lu QB, Wang T, Zhang XA, Lin SH, Lv CL, Jiang BG, *et al*: Infection and co-infection patterns of community-acquired pneumonia in patients of different ages in China from 2009 to 2020: A national surveillance study. Lancet Microbe 4: e330-e339, 2023.
5. Dear JD: Bacterial pneumonia in dogs and cats: An update. Vet Clin North Am Small Anim Pract 50: 447-465, 2020.
6. Nguyen N, Xu S, Lam TYW, Liao W, Wong WSF and Ge R: ISM1 suppresses LPS-induced acute lung injury and post-injury lung fibrosis in mice. Mol Med 28: 72, 2022.
7. Wang Y, Wang L, Ma S, Cheng L and Yu G: Repair and regeneration of the alveolar epithelium in lung injury. FASEB J 38: e23612, 2024.
8. Huang X, Zhang X, Machireddy N, Evans CE, Trewartha SD, Hu G, Fang Y, Mutlu GM, Wu D and Zhao YY: Endothelial FoxM1 reactivates aging-impaired endothelial regeneration for vascular repair and resolution of inflammatory lung injury. Sci Transl Med 15: eabm5755, 2023.
9. Morris SB, Ocadiz-Ruiz R, Asai N, Malinczak CA, Rasky AJ, Lombardo GK, Velarde EM, Ptaschinski C, Zemans RL, Lukacs NW and Fonseca W: Long-term alterations in lung epithelial cells after EL-RSV infection exacerbate allergic responses through IL-1β-induced pathways. Mucosal Immunol 17: 1072-1088, 2024.
10. Lucas R, Hadizamani Y, Gonzales J, Gorshkov B, Bodmer T, Berthiaume Y, Moehrlen U, Lode H, Huwer H, Hudel M, *et al*: Impact of bacterial toxins in the lungs. Toxins (Basel) 12: 223, 2020.
11. El Agha E and Thannickal VJ: The lung mesenchyme in development, regeneration, and fibrosis. J Clin Invest 133: e170498, 2023.
12. Zhang J, Wang T, Wang Y, Li Y, Wang L, Wang J, Miao Y, Xu F and Yao Y: Bacterial pneumonia induces senescence in resident alveolar macrophages that are outcompeted by monocytes. Cell Rep 44: 115571, 2025.
13. Wang S, Li X, Ma Q, Wang Q, Wu J, Yu H, Li K, Li Y, Wang J, Zhang Q, *et al*: Glutamine metabolism is required for alveolar regeneration during lung injury. Biomolecules 12: 728, 2022.
14. Shaghaghi H, Para R, Tran C, Roman J, Ojeda-Lassalle Y, Sun J, Romero F and Summer R: Glutamine restores mitochondrial respiration in bleomycin-injured epithelial cells. Free Radic Biol Med 176: 335-344, 2021.
15. Arribas-López E, Zand N, Ojo O, Snowden MJ and Kochhar T: The effect of amino acids on wound healing: A systematic review and meta-analysis on arginine and glutamine. Nutrients 13: 2498, 2021.
16. Stehle P, Ellger B, Kojic D, Feuersenger A, Schneid C, Stover J, Scheiner D and Westphal M: Glutamine dipeptide-supplemented parenteral nutrition improves the clinical outcomes of critically ill patients: A systematic evaluation of randomised controlled trials. Clin Nutr ESPEN 17: 75-85, 2017.
17. Kim Y, Lee JO, Lee JM, Lee MH, Kim HM, Chung HC, Kim DU, Lee JH and Kim BJ: Low molecular weight collagen peptide (LMWCP) promotes hair growth by activating the Wnt/GSK-3β/β-catenin signaling pathway. J Microbiol Biotechnol 34: 17-28, 2024.
18. Bayan R, Tauseef I, Hussain M, Ahmed MS, Haider A, Khalil AA, Islam SU and Subhan F: Fish collagen peptides' modulating effect on human skin microbiota against pathogenic *Staphylococcus aureus*. Future Microbiol 18: 795-807, 2023.
19. Czajka A, Kania EM, Genovese L, Corbo A, Merone G, Luci C and Sibilla S: Daily oral supplementation with collagen peptides combined with vitamins and other bioactive compounds improves skin elasticity and has a beneficial effect on joint and general wellbeing. Nutr Res 57: 97-108, 2018.
20. Rahabi M, Salon M, Bruno-Bonnet C, Prat M, Jacquemin G, Benmoussa K, Alaeddine M, Parny M, Bernad J, Bertrand B, *et al*: Bioactive fish collagen peptides weaken intestinal inflammation by orienting colonic macrophages phenotype through mannose receptor activation. Eur J Nutr 61: 2051-2066, 2022.
21. Hwang SB, Park HJ and Lee BH: Hair-growth-promoting effects of the fish collagen peptide in human dermal papilla cells and C57BL/6 mice modulating Wnt/β-catenin and BMP signaling pathways. Int J Mol Sci 23: 11904, 2022.
22. Ligresti G, Raslan AA, Hong J, Caporarello N, Confalonieri M and Huang SK: Mesenchymal cells in the lung: Evolving concepts and their role in fibrosis. Gene 859: 147142, 2023.
23. Andersson-Sjöland A, Nihlberg K, Eriksson L, Bjermer L and Westergren-Thorsson G: Fibrocytes and the tissue niche in lung repair. Respir Res 12: 76, 2011.
24. Doherty DF, Roets L and Krasnodembskaya AD: The role of lung resident mesenchymal stromal cells in the pathogenesis and repair of chronic lung disease. Stem Cells 41: 431-443, 2023.
25. Sveiven SN and Nordgren TM: Lung-resident mesenchymal stromal cells are tissue-specific regulators of lung homeostasis. Am J Physiol Lung Cell Mol Physiol 319: L197-L1210, 2020.
26. Thomas K, Zondler L, Ludwig N, Kardell M, Lüneburg C, Henke K, Mersmann S, Margraf A, Spieker T, Tekath T, *et al*: Glutamine prevents acute kidney injury by modulating oxidative stress and apoptosis in tubular epithelial cells. JCI Insight 7: e163161, 2022.
27. Zhao Y, Albrecht E, Stange K, Li Z, Schregel J, Sciascia QL, Metges CC and Maak S: Glutamine supplementation stimulates cell proliferation in skeletal muscle and cultivated myogenic cells of low birth weight piglets. Sci Rep 11: 13432, 2021.
28. Huang CY, Chen JK and Kuo WT: Glutamine induces remodeling of tight junctions in Caco-2 colorectal cancer cell. Med Oncol 40: 32, 2022.
29. Yang X, Zhong Y, Wang D and Lu Z: A simple colorimetric method for viable bacteria detection based on cell counting Kit-8. Anal Methods 13: 5211-5215, 2021.
30. Galindo-Feria AS, Notarnicola A, Lundberg IE and Horuluoglu B: Aminoacyl-tRNA synthetases: On anti-synthetase syndrome and beyond. Front Immunol 13: 866087, 2022.
31. Rubio Gomez MA and Ibba M: Aminoacyl-tRNA synthetases. RNA 26: 910-936, 2020.
32. Horgan CP and McCaffrey MW: The dynamic Rab11-FIPs. Biochem Soc Trans 37: 1032-1036, 2009.
33. Wilson B, Flett C, Gemperle J, Lawless C, Hartshorn M, Hinde E, Harrison T, Chastney M, Taylor S, Allen J, *et al*: Proximity labelling identifies pro-migratory endocytic recycling cargo and machinery of the Rab4 and Rab11 families. J Cell Sci 136: jcs260468, 2023.
34. Horgan CP, Hanscom SR, Jolly RS, Futter CE and McCaffrey MW: Rab11-FIP3 binds dynein light intermediate chain 2 and its overexpression fragments the Golgi complex. Biochem Biophys Res Commun 394: 387-392, 2010.
35. Shindou H and Shimizu T: Acyl-CoA:lysophospholipid acyltransferases. J Biol Chem 284: 1-5, 2009.
36. Gibellini F and Smith TK: The Kennedy pathway-de novo synthesis of phosphatidylethanolamine and phosphatidylcholine. IUBMB Life 62: 414-428, 2010.
37. Mérida I, Avila-Flores A and Merino E: Diacylglycerol kinases: At the hub of cell signalling. Biochem J 409: 1-18, 2008.
38. Yu TCY, Zhao L, Sze KMF, Tian L, Zhang VX, Lee E, Kam CS, Lee JMF, Ho DWH, Tsui YM, *et al*: GPD1L supports glycerol-3-phosphate and triacylglycerol synthesis and promotes tumor progression in HCC. Hepatology 83: 735-752, 2026.
39. Malumbres M and Barbacid M: Cell cycle, CDKs and cancer: A changing paradigm. Nat Rev Cancer 9: 153-166, 2009.
40. Fragkos M, Ganier O, Coulombe P and Méchali M: DNA replication origin activation in space and time. Nat Rev Mol Cell Biol 16: 360-374, 2015.
41. Liu X and Winey M: The MPS1 family of protein kinases. Annu Rev Biochem 81: 561-585, 2012.
42. Mannini L, Cucco F, Quarantotti V, Amato C, Tinti M, Tana L, Frattini A, Delia D, Krantz ID, Jessberger R and Musio A: SMC1B is present in mammalian somatic cells and interacts with mitotic cohesin proteins. Sci Rep 5: 18472, 2015.
43. Kroef V, Ruegenberg S, Horn M, Allmeroth K, Ebert L, Bozkus S, Miethe S, Elling U, Schermer B, Baumann U and Denzel MS: GFPT2/GFAT2 and AMDHD2 act in tandem to control the hexosamine pathway. Elife 11: e69223, 2022.
44. Wilson JE: Isozymes of mammalian hexokinase: Structure, subcellular localization and metabolic function. J Exp Biol 206: 2049-2057, 2003.
45. Rodríguez-Díaz J and Yebra MJ: Enhanced UDP-glucose and UDP-galactose by homologous overexpression of UDP-glucose pyrophosphorylase in Lactobacillus casei. J Biotechnol 154: 212-215, 2011.

46. Chen J, Cui L, Lu S and Xu S: Amino acid metabolism in tumor biology and therapy. Cell Death Dis 15: 42, 2024.
47. Riley T, Sontag E, Chen P and Levine A: Transcriptional control of human p53-regulated genes. Nat Rev Mol Cell Biol 9: 402-412, 2008.
48. Yang X and Qian K: Protein O-GlcNAcylation: emerging mechanisms and functions. Nat Rev Mol Cell Biol 18: 452-465, 2017.
49. Morales MM and Pratt MR: The post-translational modification O-GlcNAc is a sensor and regulator of metabolism. Open Biol 14: 240209, 2024.
50. Wang B and Tontonoz P: Phospholipid remodeling in physiology and disease. Annu Rev Physiol 81: 165-188, 2019.
51. Morris SM Jr: Arginine metabolism revisited. J Nutr 146: 2579S-2586S, 2016.
52. Cruzat V, Macedo Rogero M, Noel Keane K, Curi R and Newsholme P: Glutamine: Metabolism and immune function, supplementation and clinical translation. Nutrients 10: 1564, 2018.
53. Prekeris R: Rabs, Rips, FIPs, and endocytic membrane traffic. ScientificWorldJournal 3: 870-880, 2003.
54. Loughran AJ, Orihuela CJ and Tuomanen EI: *Streptococcus pneumoniae*: Invasion and inflammation. Microbiol Spectr 7: 10.1128/microbiolspec.gpp3-0004-2018, 2019.
55. Bogaert D, De Groot R and Hermans PWM: *Streptococcus pneumoniae* colonisation: The key to pneumococcal disease. Lancet Infect Dis 4: 144-154, 2004.
56. Ceccato A, Ferrer M, Barbeta E and Torres A: Adjunctive therapies for community-acquired pneumonia. Clin Chest Med 39: 753-764, 2018.
57. Gonzalez-Baro MR and Coleman RA: Mitochondrial acyltransferases and glycerophospholipid metabolism. Biochim Biophys Acta Mol Cell Biol Lipids 1862: 49-55, 2017.
58. Bradley RM, Marvyn PM, Aristizabal Henao JJ, Mardian EB, George S, Aucoin MG, Stark KD and Duncan RE: Acylglycerophosphate acyltransferase 4 (AGPAT4) is a mitochondrial lysophosphatidic acid acyltransferase that regulates brain phosphatidylcholine, phosphatidylethanolamine, and phosphatidylinositol levels. Biochim Biophys Acta 1851: 1566-1576, 2015.
59. Law SH, Chan ML, Marathe GK, Parveen F, Chen CH and Ke LY: An Updated review of lysophosphatidylcholine metabolism in human diseases. Int J Mol Sci 20: 1149, 2019.
60. Wang LM, Zhang WL, Lyu N, Suo YR, Yang L, Yu B and Jiang XJ: Research advance of Chinese medicine in treating atherosclerosis: Focus on lipoprotein-associated phospholipase A2. Chin J Integr Med 30: 277-288, 2024.
61. Subramanian K, Henriques-Normark B and Normark S: Emerging concepts in the pathogenesis of the *Streptococcus pneumoniae*: From nasopharyngeal colonizer to intracellular pathogen. Cell Microbiol 21: e13077, 2019.
62. Ogawa M, Shizukuishi S, Akeda Y and Ohnishi M: Molecular mechanism of *Streptococcus pneumoniae*-targeting xenophagy recognition and evasion: Reinterpretation of pneumococci as intracellular bacteria. Microbiol Immunol 67: 224-227, 2023.
63. Xie X, Wang Y, Yu D, Xie R, Liu Z and Huang B: DNM1, a dynamin-related protein that contributes to endocytosis and peroxisome fission, is required for the vegetative growth, sporulation, and virulence of Metarhizium robertsii. Appl Environ Microbiol 86: e01217-20, 2020.
64. Martínez RAS, Pinky PD, Harlan BA and Brewer GJ: GTP energy dependence of endocytosis and autophagy in the aging brain and Alzheimer's disease. Geroscience 45: 757-780, 2023.
65. Xu J, Liang Y, Li N, Dang S, Jiang A, Liu Y, Guo Y, Yang X, Yuan Y, Zhang X, *et al*: Clathrin-associated carriers enable recycling through a kiss-and-run mechanism. Nat Cell Biol 26: 1652-1668, 2024.
66. Settembre C, Fraldi A, Medina DL and Ballabio A: Signals from the lysosome: A control centre for cellular clearance and energy metabolism. Nat Rev Mol Cell Biol 14: 283-296, 2013.
67. Okahashi N, Nakata M, Kuwata H and Kawabata S: Streptococcus oralis induces lysosomal impairment of macrophages via bacterial hydrogen peroxide. Infect Immun 84: 2042-2050, 2016.
68. Wang Z: Cell cycle progression and synchronization: An overview. Methods Mol Biol 2579: 3-23, 2022.
69. Takénaka A and Moras D: Correlation between equi-partition of aminoacyl-tRNA synthetases and amino-acid biosynthesis pathways. Nucleic Acids Res 48: 3277-3285, 2020.
70. Walter P and Ron D: The unfolded protein response: From stress pathway to homeostatic regulation. Science 334: 1081-1086, 2011.
71. Geng P, Qin W and Xu G: Proline metabolism in cancer. Amino Acids 53: 1769-1777, 2021.
72. Krishnan N, Dickman MB and Becker DF: Proline modulates the intracellular redox environment and protects mammalian cells against oxidative stress. Free Radic Biol Med 44: 671-681, 2008.
73. Cao J, Li M, Liu K, Shi X, Sui N, Yao Y, Wang X, Li S, Tian Y, Tan S, *et al*: Oxidative phosphorylation safeguards pluripotency via UDP-N-acetylglucosamine. Protein Cell 14: 376-381, 2023.
74. Nishikawa A, Karita S and Umekawa M: Ngk1 kinase-mediated N-acetylglucosamine metabolism promotes UDP-GlcNAc biosynthesis in Saccharomyces cerevisiae. FEBS Lett 598: 1644-1654, 2024.
75. Alteheld B, Evans ME, Gu LH, Ganapathy V, Leibach FH, Jones DP and Ziegler TR: Alanylglutamine dipeptide and growth hormone maintain PepT1-mediated transport in oxidatively stressed Caco-2 cells. J Nutr 135: 19-26, 2005.
76. Xu G, Zhao W and Yu Z: Intestinal epithelial transport of bioactive di/tripeptides through PepT1: Molecular mechanism and influencing factors. Food Chem 496: 146851, 2025.
77. Spanier B and Rohm F: Proton coupled oligopeptide transporter 1 (PepT1) function, regulation, and influence on the intestinal homeostasis. Compr Physiol 8: 843-869, 2018.
78. Paneque A, Fortus H, Zheng J, Werlen G and Jacinto E: The hexosamine biosynthesis pathway: Regulation and function. Genes (Basel) 14: 933, 2023.
79. Zhu Q, Cheng X, Cheng Y, Chen J, Xu H, Gao Y, Duan X, Ji J, Li X and Yi W: O-GlcNAcylation regulates the methionine cycle to promote pluripotency of stem cells. Proc Natl Acad Sci USA 117: 7755-7763, 2020.
80. Chen CL, Hsu SC, Ann DK, Yen Y and Kung HJ: Arginine signaling and cancer metabolism. Cancers (Basel) 13: 3541, 2021.
81. Wyant GA, Abu-Remaileh M, Wolfson RL, Chen WW, Freinkman E, Danai LV, Vander Heiden MG and Sabatini DM: mTORC1 activator SLC38A9 is required to efflux essential amino acids from lysosomes and use protein as a nutrient. Cell 171: 642-654.e12, 2017.
82. Wu Z, Hou Y, Dai Z, Hu CA and Wu G: Metabolism, nutrition, and redox signaling of hydroxyproline. Antioxid Redox Signal 30: 674-682, 2019.
83. Swanson D, Block R and Mousa SA: Omega-3 fatty acids EPA and DHA: Health benefits throughout life. Adv Nutr 3: 1-7, 2012.
84. Kousparou C, Fyrilla M, Stephanou A and Patrikios I: DHA/EPA (Omega-3) and LA/GLA (Omega-6) as bioactive molecules in neurodegenerative diseases. Int J Mol Sci 24: 10717, 2023.
85. Kostadinova E, Chaput C, Gutbier B, Lippmann J, Sander LE, Mitchell TJ, Suttorp N, Witzenrath M and Opitz B: NLRP3 protects alveolar barrier integrity by an inflammasome-independent increase of epithelial cell adherence. Sci Rep 6: 30943, 2016.
86. Cui L, Yang R, Huo D, Li L, Qu X, Wang J, Wang X, Liu H, Chen H and Wang X: *Streptococcus pneumoniae* extracellular vesicles aggravate alveolar epithelial barrier disruption via autophagic degradation of OCLN (occludin). Autophagy 20: 1577-1596, 2024.
87. Sura T, Gering V, Cammann C, Hammerschmidt S, Maaß S, Seifert U and Becher D: *Streptococcus pneumoniae* and influenza A virus co-infection induces altered polyubiquitination in A549 cells. Front Cell Infect Microbiol 12: 817532, 2022.
88. Jones DL, Morley MP, Li X, Ying Y, Zhao G, Schaefer SE, Rodriguez LR, Cardenas-Diaz FL, Li S, Zhou S, *et al*: An injury-induced mesenchymal-epithelial cell niche coordinates regenerative responses in the lung. Science 386: eado5561, 2024.
89. Xin S, Ding Y, Yu T, Fu Y, Cui Y and Nie H: Mesenchymal stem cell-secreted KGF ameliorates acute lung injury via the Gab1/ERK/NF-κB signaling axis. Cell Mol Biol Lett 30: 79, 2025.
90. Ushakumary MG, Riccetti M and Perl AT: Resident interstitial lung fibroblasts and their role in alveolar stem cell niche development, homeostasis, injury, and regeneration. Stem Cells Transl Med 10: 1021-1032, 2021.
91. Kang H, Kim OH, Chang ES, Kim J, Kim JY, Shin GS, Kim CH, Lim Y, Seo YJ, Kim JW and Lee HJ: Enhanced engraftment and immunomodulatory effects of integrin alpha-2-overexpressing mesenchymal stromal cells in lipopolysaccharide-induced acute lung injury. Stem Cell Res Ther 16: 286, 2025.

92. van der Koog L, Boerrigter MJ, Gorter IC, Gosens R and Nagelkerke A: Lung fibroblast-derived extracellular vesicles and soluble factors alleviate elastase-induced lung injury. Eur J Pharmacol 974: 176612, 2024.
93. van der Koog L, Woest ME, Gorter IC, Verschut V, Elferink RAB, Zuidhof AB, Nugraha DF, Koloko Ngassie ML, Bos SIT, Dhakad D, *et al*: Fibroblast-derived osteoglycin promotes epithelial cell repair. NPJ Regen Med 10: 16, 2025.
94. Ren W, Xia Y, Chen S, Wu G, Bazer FW, Zhou B, Tan B, Zhu G, Deng J and Yin Y: Glutamine metabolism in macrophages: A novel target for obesity/type 2 diabetes. Adv Nutr 10: 321-330, 2019.
95. Liu PS, Wang H, Li X, Chao T, Teav T, Christen S, Di Conza G, Cheng WC, Chou CH, Vavakova M, *et al*: α-ketoglutarate orchestrates macrophage activation through metabolic and epigenetic reprogramming. Nat Immunol 18: 985-994, 2017.